Structural and petrological characteristics of a Jurassic detachment fault from the Mont-Blanc massif (Col du Bonhomme area, France)

Nicolas Dall'Asta, Guilhem Hoareau, Gianreto Manatschal, Stephen Centrella, Yoann Denèle, Charlotte Ribes, Amir Kalifi

Structural and petrological characteristics of a Jurassic detachment fault from the Mont-Blanc massif (Col du Bonhomme area, France)

Nicolas Dall'Asta[*1], Guilhem Hoareau[1], Gianreto Manatschal [2], Stephen Centrella[1], Yoann Denèle[3], Charlotte Ribes[4], Amir Kalifi[1,4]

[1] Université de Pau et des Pays de l'Adour, E2S UPPA, CNRS, LFCR-France
[2] Université de Strasbourg, CNRS, ITES UMR 7063, Strasbourg F-67084, France
[3] Géosciences Environnement Toulouse, Université de Toulouse, CNRS, IRD, UPS, CNES, F-31400 Toulouse, France
[4] TotalEnergies SE - Centre Scientifique et Technique Jean Féger (CSTJF) – TOTAL – France

*Corresponding author: Nicolas Dall'asta
+33 0638955492 (France)
nicolas.dallasta@univ-pau.fr
LFCR
Avenue de l'Université
64012 PAU

Keywords: Alpine Tethys, Detachment fault, Mont-Blanc massif, Grès Singuliers, Necking domain

Abstract

Necking zones, located between the proximal and distal domains of passive margins, are characterized by important crustal thinning and the occurrence of extensional detachment faults. Here we provide a petrographic, microstructural and geochemical study of an extensional detachment fault discovered in the Mont-Blanc massif, which was located in the necking zone of the European margin during Early Jurassic rifting. The footwall of the fault consists of basement gneisses, while its hanging wall presents pre- to syn-rift deposits. A careful observation of the basement / cover contact also reveals the presence of a strain gradient affecting the Variscan gneisses, which are progressively deformed to cataclasite and to black gouges at the top basement, and sealed by undeformed Jurassic syn-rift sandstones, the Grès Singuliers, which rework fault rock pebbles. Microscale observations also indicate fluid-assisted deformation, characterized by the total breakdown of feldspars and the coeval formation of white mica, leading to strain softening along the fault plane. The overall observations point toward a rift-related detachment fault responsible for the exhumation of the internal Mont-Blanc basement, an interpretation which challenges previous models of crustal exhumation in the External massifs of the Alps. Finally, the preservation of an undeformed syn-rift sedimentary cover sealing a tectonized top basement makes this area a fossil analogue for detachment faults in necking domains. It demonstrates that preservation of pre-Alpine, rift related structures is possible even in highly deformed areas, and emphasizes the role played by pre-Alpine inheritance on the building of the Alpine Mountain belt.

Introduction

Recent investigations suggest that orogens resulting from a Wilson cycle (Wilson 1966; Wilson et al., 2019) are strongly controlled by rift-related inheritance (e.g., Jammes and Huismans, 2012; Chenin et al., 2017; Jourdon et al., 2019). Such inheritance is largely responsible for the position of major decoupling levels that can be reactivated during convergence, and thus control the final architecture of the orogen, as recently demonstrated for the Pyrenean system (Cadenas et al., 2018; Espurt et al., 2019; Izquierdo-Llavall et al., 2020; Labaume and Teixell, 2020; Lescoutre and Manatschal, 2020; Manatschal et al., 2021) or the eastern Alps (Mohn et al., 2011; Mohn et al., 2014). Paleogeographic reconstructions suggest that the same may apply to the Western Alps (Mohn et al., 2011). Indeed, the present-day External Crystalline Massifs (ECM) are located at the transition between the

proximal and the distal domains of the former European margin, which formed during Jurassic rifting and hyperextension (Mohn et al., 2014). However, little work has yet been done on rift-related, pre-Alpine structures in the internal part of the ECM, and their possible impact on the subsequent Alpine reactivation (Butler, 1986, 2017). Jurassic rift-related faults were identified such as the Ornon fault (Belledonne massif; Barfety and Gidon, 1984; Lemoine et al., 1986) or inferred from variations in the thickness of lower Jurassic sedimentary rocks on either side of the ECM (Lemoine and Trümpy, 1987; Bellahsen et al., 2012; Bellahsen et al., 2014), and interpreted as a high-angle normal fault associated with limited crustal thinning. The geometry of these faults contrasts with the large offset normal faults expected at the transition between the proximal and distal domains, as observed at present-day rifted margins (e.g. Osmundsen and Péron-Pinvidic, 2018). Recently, Ribes et al.(2020) proposed the presence of a rift-related, Jurassic detachment fault in the internal Mont-Blanc massif, responsible for the tectonic exhumation of the basement leading to a local emersion and reworking of the Variscan basement in the sediment, as documented in the Lower Jurassic sandstones of the Grès Singulier Formation. The occurrence of such a detachment system predicts important crustal thinning, which is not only in accordance with observations made at present-day rifted margins (Osmundsen and Péron-Pinvidic, 2018; Muñoz-Barrera et al., 2020; Ribes et al., 2020) but is also compatible with the subsidence history observed at the transition between the proximal and distal domains in the Alpine domain (Masini et al., 2014; Ribes et al., 2019b). However, this interpretation is mostly based on field structural and sedimentological observations, calling for a more detailed structural, petrological, and geochemical characterization of the detachment fault previously proposed by Ribes et al. (2020). Corroborating the existence of such a detachment surface is not only important for the understanding of the pre-Alpine evolution and the structure of the European margin, but it also strongly impacts the interpretation of the Alpine orogenic evolution. Its existence would have major implications for the evolution of the Mont Blanc Massif and on a larger scale for the interpretation of how the transition between the internal and external parts of the Western Alps can be interpreted and how far they are linked/controlled by rift inherited structures.

In this contribution, we focus on the Col du Bonhomme area, where the proposed detachment surface has been described in most detail by Ribes et al. (2020). Field, microstructural and petrological observations, and elemental geochemical analyses are used

to elucidate the kinematics, the mineralogical and geochemical characteristics, and the relative timing of this structure. Our aim is to determine whether this structure was inherited from Jurassic rifting or if it has an Alpine origin.

1. Geological setting

The Alpine orogen was formed as a result of the closure of the Alpine Tethys since the Cretaceous. Its evolution is linked with a complex, polyphase kinematic evolution leading to the subduction of the oceanic, proto-oceanic and exhumed subcontinental mantle domains and the subsequent collision of the Jurassic Adriatic and Europe margins (Ford et al., 2004; Rosenbaum and Lister, 2005; Fig.1). Several studies pointed out the link between the main Alpine tectonic units, and the fossil rift domains of the Alpine Tethys (Argand, 1916; Debelmas and Lemoine, 1970; Lemoine et al., 1986; Lemoine and Trümpy, 1987; Stampfli and Hochard, 2009; Bellahsen et al., 2014; Mohn et al., 2014). Indeed, wide-spread Jurassic rifting, which initiated with distributed extension during the Early Jurassic (e.g. Bourg d'Oisans basin, Lemoine et al., 1981; Barfety and Gidon, 1984; Chevalier, 2002), resulted in a complex arrangement of hyperextended, exhumed mantle and proto-oceanic domains (e.g., Valais and Liguro-Piemont domains of Dumont et al., 1984; Lemoine and Tricart, 1986; Lagabrielle, 1987; Bousquet et al., 2002; Schmid et al., 2004; Loprieno et al., 2011; Beltrando et al., 2012; Ribes et al., 2019c) during the late Middle Jurassic to Cretaceous. The external units (Jura, Bauges, Bornes, Chartreuse, Vercors) have been commonly assigned to the proximal domain of the former European margin (Fig.1 A,B,C,D; Tricart et al., 2000). They are characterised by the presence of high-angle normal faults of lower Jurassic age associated to half-graben type basins filled with shallow marine sediments (Lemoine et al., 1981). In contrast, the internal units originate from the distal part of the European margin, corresponding to the hyperextended domain, the exhumed mantle and the oceanic domain. Due to important Alpine tectonic overprint, most of the distal parts of the margin have been intensively deformed during subduction (e.g. Pré Piémont domain Pantet et al., 2020), collision and subsequent exhumation (e.g. oceanic domain HP-LT Schistes Lustrés units (Elter, 1971; Lagabrielle et al., 2015). Consequently, rift-related structures are only preserved in a few places (e.g. Petit Saint Bernard (Beltrando et al., 2012); Tasna (Ribes et al., 2019c), Chenaillet (Manatschal et al., 2011), Aiguille Rouge D'Arolla (Decrausaz et al., 2021). A key result of these studies is that the external and

internal units show contrasting features not only in their stratigraphic and metamorphic imprint, but also in their inherited structures with major implications for their Alpine tectonic history.

The ECM (e.g., Aar, Mont-Blanc, Belledonne, Pelvoux, Argentera Massifs), which belong to the external units of the Alps, are commonly interpreted to derive from the transition between the proximal and distal domains of the European margin (former necking domain; Butler, 1986; Butler,1989; Mohn et al., 2014; Fig.1C and D). At present, they floor the Helvetic and Penninic nappes (Fig.1B), and reached greenschist P-T conditions during Alpine nappe stacking (Bousquet et al., 2008; Rosenberg et al., 2021). Most of the rift-related structures have been overprinted by Alpine deformation, as for example the reactivation of former normal faults in the Aar massif (Nibourel et al., 2021). Therefore, most of the rift history has been deduced from the facies, thickness and paleo bathymetric evolution of the syn- and post-rift deposits (e.g., Sangle unit; Epard, 1990 and Ultrahelvetic units; Trumpy, 1951) and from the difference of geometry between large fold and thrust nappes (e.g., Vervex unit (Epard, 1990) or Morcles-Doldenhorn nappe (Kiss et al., 2020)).

The Mont-Blanc Massif, which is part of the ECM, is a Variscan polymetamorphic basement made up of paragneisses, cordierite-bearing migmatites and granitic intrusions in its western part (external Mont-Blanc massif), and by a large pluton of metaluminous, ferro-potassic granite surrounded by migmatites in its eastern part (internal Mont-Blanc massif; Bussy, 1990). The pluton corresponds to a post-orogenic magmatism related to extensional tectonic (orogenic collapse or back-arc extension), with a mantle-derived source associated to crustal contamination (Bussy et al., 2001). U-Pb dating of the cordierite-bearing leucosomes and of the granites showed that this late Carboniferous magmatic event lasted about 10 Ma in the ECM (migmatization took place at ca. 307 ± 2 Ma and granite emplacement between 307±3Ma (Montenvers granite) and 303 ± 2 Ma for the Mont-Blanc granite (Bussy et al., 2001)). The absence of a clearly defined metamorphic contact aureole around the Mont-Blanc granite, noted by Bussy (1990), may indicate an emplacement at significant depth, with pressures up to 3.8 kbar at the top of the intrusion, i.e., an assumed intrusion depth at 9 to 12 km for the pluton roof (Marshall et al., 1997). Cooling ages and P-T conditions were obtained from skarns located immediately around the granite (i.e., on the pluton walls), providing temperatures of 400/500°C and pressures of 4/8 kbar (based on Ti thermometry on amphibole and stable isotopes) in Mont-Chemin ore deposits, dated at 303-

335 Ma using Ar/Ar on amphiboles (Marshall et al., 1997). Most studies assumed that post-Variscan exhumation to the surface of the external Mont-Blanc Massif was achieved during the Permian (Marshall et al., 1997). It was followed by the development of a Permo-Triassic erosional surface, as observed in the external Mont-Blanc Massif and the Aiguille-Rouge Massif located westward (Epard, 1986). In the western areas, the exhumation was further constrained by the occurrence of Ladinian to Carnian tidal sandstones (Demathieu and Weidmann, 1982) known as the Vieux Emosson Formation (Epard, 1989) directly overlying the basement. Upper Triassic dolostones and evaporites (Arrandellys Fm. ; Epard, 1989) complete the Triassic sequence.

The conditions of exhumation in the internal Mont-Blanc Massif are more debated. Most studies considered that similarly to the external part of the massif, the Triassic deposits form a primary, stratigraphic contact with the eroded basement (Eltchaninoff-Lancelot et al., 1982; Epard, 1990). In contrast, Ribes et al. (2020) have proposed that the contact between the pre-rift deposits and the basement corresponds to a Jurassic detachment fault, i.e., that they are allochthonous relative to the underlying exhumed basement. A key observation is the presence of early syn-rift sandstones (Sinemurian/Pliensbachian) corresponding to the Grès Singuliers Formation (Landry, 1976; Eltchaninoff, 1980; Epard, 1989; Ribes et al., 2020) that overlies a deformed and exhumed basement (Fig. 2). These sandstones, up to 50 meters thick, have been interpreted as the result of local uplift and erosion of the Mont Blanc basement associated either with a normal fault (Epard, 1990; Meyer, 2002), or a large offset extensional detachment fault (Ribes et al., 2020). Ribes et al. (2020) proposed that exhumation and related uplift of the internal Mont Blanc basement occurred during rift-related necking at around 185 ± 5 Ma (Pliensbachian), resulting in sub-areal exposure of a core complex type structure. It is interesting to note that the Mont-Blanc core complex of Ribes et al. (2020) can be well compared to the Mont-Blanc island whose presence was proposed and discussed in Trümpy (1971) and Loup (1992) to explain the occurrence of the Grès Singuliers and its primary contact with the basement. During the Aalenian transgression, the core complex/island was drowned and the Triassic to lower Jurassic deposits were covered by Aalenian to Oxfordian black shales of the Dugny Formation (Lemoine et al., 1986; Meyer, 2002, Fig.2). These were followed by Upper Jurassic to Cretaceous limestones.

In the Mont-Blanc massif, the Alpine deformation corresponds to: (i) the thrusting of the more internal Helvetic and Penninic nappes over the Mont-Blanc during the Late Eocene to Early Miocene (Leloup et al., 2005; Egli and Mancktelow, 2013); followed by (ii) thick-skin deformation leading to the closure of the Morcles basin (Escher et al., 1993; Herwegh and Pfiffner, 2005) ; and (iii) to thrusting of the Mont-Blanc basement over the Aiguille-Rouges basement (Mont-Blanc shear zone) from middle Miocene to early Pliocene (Leloup et al., 2005). This thrusting was associated with the back thrusting of the basement over sediments along the eastern/internal border of the Massif (Guermani and Pennacchioni, 1998; Leloup et al., 2005; Egli and Mancktelow, 2013). Studies of metamorphic assemblages (muscovite-biotite-chlorite-epidote), U-Th-Pb geochronology on allanite and Ar/Ar geochronology on phengite, biotite and phlogopite indicate that the Alpine metamorphic peak was reached between 28 and 15 Ma, with pressures of 0.5 GPa and temperatures up to 400°C in the basement (Rolland et al., 2003; Rolland et al., 2008; Cenki-Tok et al.,2014). It was followed by Neogene to present day exhumation of the massif (Glotzbach et al., 2008; Boutoux et al., 2016; Herwegh et al., 2020).

In this study, we focus on the Col du Bonhomme area located to the NW of Bourg St-Maurice (France). It corresponds to an antiformal fold (Fig.1E) preserving the cover of the southern Mont-Blanc Massif below the Helvetic nappes, thus giving access to the pre-Alpine contacts. In this area (Fig.2B), the syn-rift Grès Singuliers lie unconformably above the pre-rift Triassic cover and the basement. The nature, age, and significance of the contact between the sedimentary cover and the basement is the main goal of our study.

2.Methodology

The geological maps of Meyer (2002) and Ribes et al. (2020), complemented by Google Earth satellite images, field observations and drone acquisitions, were used to build a new 11 km² map of the area (Fig.2). Field observations were focused on the facies and thickness distribution of the syn- and pre-rift sedimentary cover, their relationship with the basement, as well as on the recognition and structural characterization of different fault generations and related fault rocks (cataclasites, fault breccias and gouges). In total 71 samples were collected (33 fault rocks; 33 samples from the sedimentary cover and 5 from the unfractured basement).

In order to quantify the peak metamorphic temperatures reached during Alpine metamorphism in the Col du Bonhomme area, Raman spectroscopy of carbonaceous material (RSCM) analyses were performed on 2 polished thin sections of organic-rich Aalenian shales and one section of pre-rift limestone. A total of 55 Raman spectra were acquired with a Horiba Jobin-Yvon Labram II spectrometer coupled to a microscope, at the Institut des Sciences Moléculaires, Université de Bordeaux, France. Acquisitions parameters include a 514.5 nm argon laser, an extended scanning mode (500-2000cm^{-1}) and an acquisition time of 30s. Spectra of the first-order region of carbonaceous material were processed using the Fityk software (Wojdyr, 2010). Each spectrum was fitted with 4 bands (D1, D2, D3, and the graphite band G) with Voigt profiles. The calibration of Beyssac et al. (2002), based on the parameter R2 = D1/(G + D1 + D2) was used.

Petrographic observations of polished thin sections from sampled rocks (n = 71) were performed with a Nikon LV150ND optical microscope, and by cathodoluminescence (CL) using a Cathodyne system (OPEA) with an operating condition of 15 kV–18 kV and a gun current of 300–350 mA under a 60 mTorr vacuum (LFCR, Pau, France). Other techniques include a Zeiss EVO50 scanning electron microscope (SEM) coupled to EDS mapping (20kV beam; PLACAMAT, Pessac, France). Electron Probe Micro-Analyzer (EPMA) analyses were carried out on polished thin sections using a Cameca SXFive instrument at the Centre de Microcaractérisation Raymond Castaing in Toulouse (France), calibrated with natural and synthetic in-house standards: aluminium oxide (Al), wollastonite (Si, Ca), sanidine (K), manganese titanite (Mn), hematite (Fe), albite (Na), barite (Ba), celestine (Sr). For the determination of major element compositions on silicate from the fault rocks and phosphate in the basement minerals, the operating conditions were set at 15 kV, with a probe current of 50 nA, and a 2 µm beam. For elemental mapping, similar conditions, and a step size of 2 µm were used.

Following microscopic acquisitions, the XMapTools software (Lanari et al., 2014; Lanari et al., 2019) was used to build quantitative X-ray electron microprobe maps, and the AX software (Holland and Powell, 2006) to recalculate the structural formulas of the different mineral phases observed. Optical photomicrographs of the fault rocks were processed with ImageJ (Rasband, 1997) to calculate the surface area, the orientation and the circularity of each grain, and the detection of microfractures. Grain size was calculated using the equal area diameter. These parameters were used to calculate several fault parameters

such as the fractal dimension β, the cut-off sharpness α and the characteristic diameter D_c (μm), by fitting the curve obtained with the equation $P\left(\frac{N}{N_t}\right) = (1 + \left(\frac{D}{Dc}\right)^{\alpha})^{\frac{-\beta}{\alpha}}$ (Otsuki, 1998; Monzawa and Otsuki, 2003), with P the number of grains (N) larger than a certain diameter (D in μm) with N_t the total number of grains. Similarly, the microfracture density (μm^{-1}) was calculated using the circle inventory method (Davis et al., 2011; Rossetti et al., 2010), consisting in dividing the total length of microfractures within a circle by the area of this circle.

3.Results

3.1 Alpine metamorphic peak in the Col du Bonhomme area

The peak temperatures calculated from the RSCM analyses of the Aalenian shales and pre-rift limestone samples are 322 ± 18 °C, 336 ± 25 °C and 335 ± 22°C (Table1 and table S1, S2, S3). Since these shales are rich in organic carbon and are post-tectonic relative to the rifting in the Mont-Blanc/proximal domain, these values likely correspond to the peak temperatures reached during the Alpine metamorphic overprint. These results, which point to lower greenschist facies conditions, are in good agreement with illite crystallinity values measured in the area (1.35; Eltchaninoff and Triboulet, 1980), and with the compilation of RSCM data by Rosenberg et al. (2021), giving a temperature below 350°C for the southern part of the Mont-Blanc area. Petrographic observations on the Grès Singuliers highlight the impact of such metamorphism on the mineralogy of the Jurassic deposits in the internal Mont Blanc Massif where alpine metamorphism resulted in a static thermal overprint marked by overgrowth of muscovite over illite (Fig. S4).

3.2 Macroscopic description of the basement / sediment contact

In the Col du Bonhomme area, the contact between the Mont-Blanc basement and the overlying Triassic and Liassic sediments crop out at several places as shown in Figure 2.

3.2.1. Basement and tectonized top basement

The basement is composed of a cordierite bearing migmatitic gneiss with a sub-vertical NNE-SSW striking foliation (Fig. 3G). It is intruded by meter-thick magmatic bodies corresponding to aplite.

Towards the top of the basement, the gneiss is progressively deformed over about 40 meters, showing a gradational transition from the well-preserved gneiss to a cataclasite and a gouge at the basement/cover contact (Fig. 3). Locally, sub-horizontal foliation is visible, possibly corresponding to Variscan mylonites cross-cutting the sub-vertical foliation. They are parallel to the top basement contact (Fig.3 A, F and G) and show a brittle overprint forming tectonic breccia. In more detail, the damaged gneiss is characterized by a network of anastomosed fault zones of cataclastic gneiss with lenses/clasts of preserved gneiss (Fig. 3A), that we define as the damage zone. These anastomosing fault zones form a progressively denser network towards the top, clearly showing a strain gradient toward the top basement. The leucosomes of the migmatitic gneiss are good markers for the strain at the macroscale. Far from the contact, the initial texture of the leucosomes is preserved. Upsection, they are affected by important, centimetre scale fractures without displacement, indicating an increase of the brittle overprint toward the basement/sediment contact (Fig.3E). Closer to the contact (< 10 m Fig.3A), the fracture network becomes denser, the fragments of leucosomes get smaller and gradually develop into cataclasites. The brittle overprint of the former host rock includes the disaggregation of the fabric and the alteration of the feldspars, leading to an increase of the phyllosilicate content upsection. Kinematic markers of fault-related structures are sparse and commonly difficult to interpret. They mainly consist of few lineations giving a N-S direction. In phyllosilicate-rich zones, the kinematics is clearer as the foliation is more marked. S/C' structures are observed, where the C' plane has an orientation 200/36 with a top to the SSW sense of shear.

The core of the fault (i.e., the core zone; < 1 meter-thick, Fig. 3A and C) corresponds to a matrix-supported fault rock with a high content of phyllosilicates, here referred to as indurated gouge. It appears as a dark, fine grained discontinuous layer with a well-developed foliation. It forms a sharp contact with the underlying cataclasites forming the damage zone (Fig. 3A). Centimetric injections of material from the gouge are visible in the cataclasite (Fig. 3A). Veins parallel to the foliation are also observed (Fig.3C). The gouge has the same appearance at the macro and micro-scale with the alternation of matrix-rich and clast-rich bands, showing N-S lineated clasts (Fig. 3F).

3.2.2. Pre-rift, tectonized sedimentary deposits

Pre-rift sediments locally lie above the tectonized basement. Four types can be distinguished, whose spatial distribution is variable along the contact. The first one, which is common, corresponds to discontinuous 20 cm-thick lenses of sandstones composed of micrometric angular lithic fragments and carbonate clasts within a calcite cement (Fig. 3C). The second type consists to a limestone containing millimetric to centimetric, euhedral quartz crystals with 100µm-large rectangular anhydrite inclusions (*Fig. S5*). The third type corresponds to upper Triassic brownish dolostone (Arandellys Fm.), whose thickness ranges from 0 to approximately 10 meters, and which covers the sandstone lenses and limestones with quartz nodules (Fig. 2,3A and 3C). Although the dolostone origin is sedimentary, it is now significantly deformed up to forming both, metric asymmetric boudins and monomictic breccias. The dolostone layers form an angle of about 10-15° with the tectonic contact separating the basement from the pre-rift sediments suggesting an angular unconformity. In addition, the dolostone boudins can lie directly above the tectonized basement and are associated with tectonic breccias. These breccias are either polymict containing angular to sub-angular pluri-cm to pluri-dm clasts of both dolostones and basement or monomict (*Fig. S6 A, B)* including dolostone and minor quartz-bearing limestone clasts characterized by a jigsaw geometry (*Fig. S6 C, D*). Clasts of dolostone embedded in the gouge are frequently observed (*Fig. S6 E and F*). Finally, the fourth type of pre-rift sediments includes Lower Jurassic (Hettangian) calcschists and limestones preserved in the Rocher du Bonhomme.

3.2.3. Syn-rift sediments sealing the contact

At some places, the gouge and cataclasites within the top basement are crosscut by subvertical cracks, which are filled with a sedimentary breccia containing cataclastic material, clasts of gouges and quartz veins floating in a brownish matrix (Fig. 4). The cracks are tens of cm-large and deep and can be best interpreted as neptunian dykes (Fig. 4A). The brown sedimentary infill corresponds to a calcite-rich indurated mud containing quartz grains and bioclasts, mostly crinoids (Fig. 4C, D). The same matrix is also locally observed above the basement gouge and is found within the cracks (Fig. 4B). This observation suggests that the meter-thick brown breccia made mainly of basement clasts, forms a stratigraphic contact with the tectonized basement.

The pre-rift dolostones and limestones are truncated by an erosional surface at its top, and are unconformably overlain, along a stratigraphic contact, by Liassic syn-rift sandstones

and conglomerates of the Grès Singuliers Fm (Fig. 2,3 and S5 F). These sandstones, 10 to 30 meters thick, can also seal directly the tectonized basement at places where the pre-rift deposits are absent. The lower part of the Grès Singuliers corresponds to: (i) monomictic conglomerates (pluri-dm angular carbonate pebbles derived from the pre-rift limestones and dolostones), with a N-S paleocurrent direction as deduced from pebble imbrications different from the NW-SE paleocurrent measurements from the upper part of the formation (Ribes et al., 2020), or (ii) polymictic conglomerates (sub-angular to rounded pebbles of carbonates and basement). Pebbles of cataclasites are also observed (45°43'46.41''N/ 6°43'47.96''E), indicating reworking of the fault rocks from the underlying exhumed basement (Fig.3) into the sediments. The upper part of the Grès Singuliers corresponds to shoreface and foreshore sandstones with strong tidal influence (Ribes et al., 2020). Well-preserved sedimentary figures such a cross beds, small tidal laminations and bioturbations are common.

At the top of the Formation, NW-SE stretching lineations related to Alpine deformation are commonly associated with millimetre-thick proto-mylonite shear zones and a pervasive cleavage. Above the sandstones, Aalenian shales belonging to the Dugny Fm. show important deformation with C/S structures giving a top to the NW sense of shear (Fig. 3F). These structures correspond to the decollement level of the Helvetic nappes above the Mont-Blanc massif (Eltchaninoff-Lancelot et al., 1982; Egli and Mancktelow, 2013). It is important to note that the base of the Grès Singuliers is little deformed and that there is a clear strain gradient upsection towards the main Alpine thrust.

3.2.4. High-angle faults

Both the basement and the pre-rift deposits are offset by two sets of high-angle normal faults, one striking NE-SW and the second NW-SE. The NE-SW striking normal faults show small offsets (few meters) of the top basement. The NW-SE faults offset the basement and the pre-rift but also the Grès Singuliers and the Aalenian shales. In the Col des Fours area, a NW-SE fault (30/45) offsets the top basement, including the gouges and cataclasites, by about 35 m (Fig. 5). A sedimentary wedge (15°) formed by the Grès Singuliers is visible in the hanging wall of the fault (Fig. 5). Thickening of the sandstones toward the fault plane is compatible with the Grès Singuliers being syn-tectonic to this fault and suggesting a fault activity being Pliensbachian-Toarcian. A roll-over anticline (fold axis 100/14) accommodates

385 the deformation of the pre-rift cover. Slickensides on planes parallel to the fault strike (pitch
386 of 18°) and on secondary planes oblique to the fault (strike: N150) show an important strike-
387 slip component, possibly related to an Alpine reactivation of the fault (coherent with the
388 WSW strike slip direction measured in the area by Egli and Mancktelow, 2013, in the Helvetic
389 cover).
390
391 **3.2.5. Synthesis of macroscopic observations**
392 A strain gradient is observed in the basement toward its top. Variscan foliation is
393 overprinted by brittle deformation, leading to cataclasite and gouge formation. This
394 progressive localisation of the deformation is marked by an increase in the content of
395 phyllosilicates which make most of the gouges. This tectonized basement is overlaid by pre-
396 rift and syn-rift sediments, but the nature of the relationship between basement and its
397 sedimentary cover differs between both types. The pre-rift/basement contact is tectonic
398 while the syn-rift/basement contact is stratigraphic. Therefore, the syn-rift deposits seal an
399 exhumed tectonized top basement, as well as its overlying pre-rift sediments. The syn-rift
400 Grès Singuliers, are affected by a strain gradient as can be seen at its top, which increases
401 toward the overlying Aalenian shales. This alpine deformation is the most intense in the
402 Aalenian shales, which acted as an important decollement during emplacement of the
403 Helvetic nappes (Eltchaninoff-Lancelot et al., 1982; Egli and Mancktelow, 2013).
404
405 **3.3 Petrological and microstructural observations**
406 **3.3.1 Host rock: Variscan gneiss**
407 At distance from the tectonic contact, the subvertical foliation of the migmatitic
408 gneiss basement (quartz (43%), biotite (18%), and feldspar (37%), Fig.6) is highlighted by by
409 the alternation of biotite and quartz-feldspar bands. Accessory minerals are mostly
410 fluorapatite found with biotite. Leucosomes related to melt infiltration are parallel to the
411 gneiss foliation. They are composed of coarse quartz and feldspars. Micro textural analysis
412 shows that quartz grains were affected by grain boundary migration (GBM) and sub-grain
413 rotation with the myrmekitization of some plagioclase feldspars. The migmatites are
414 intruded by aplite veins characterised by a high amount of quartz. The latter are typical of
415 high temperature rock fabrics of migmatitic gneisses.

The high temperature (HT) gneiss fabric is also overprinted by microfractures affecting the feldspars, locally forming micro veins showing bulging recrystallisation where the fractures propagate in the quartz. These fractures are mostly transgranular and crosscut the previous HT foliation. They are associated with alteration of feldspars with formation of white micas, albite and microporosity (Fig.7A). Small kinks and crenulation with rutile-rich micro fractures highlight the deformation in the phyllosilicate-rich zones (Fig.7B). This deformation is associated with hydration of the host rock leading to alteration of feldspar and biotite and the formation of white micas. Primary biotite is strongly altered with formation of chlorite and rutile. Alteration is stronger on the border of the crystals and along their cleavage, where rutile is observed, whereas the core of the crystals is better preserved. Chlorite corresponds to an intermediate composition between chlinochore, Fe-sudoite and amnesite (Table 2). The paragenetic association of the hydration of the host rock is K-Fsp + Ab + Bi ↔ Chl + Mu + Rt ± Qtz with a total amount of phyllosilicate of around 10%.

3.3.2 Damaged zone

In the damage zone, the gneiss protolith is highly altered and affected by brittle deformation. It is composed mainly of quartz, plagioclase and K-feldspars, white micas, sulphides (pyrite and arsenopyrite) and iron oxide minerals. Minerals inherited from the gneiss protolith correspond to quartz, remnants of feldspars and small zircons. Chlorite, fluorapatite and biotite, which were present further away from the tectonic contact, are absent. This fabric is overprinted by fractures filled mostly with iron oxide.

In the outer damage zone (>20 m), feldspar constitutes 30% of the rock (10% for plagioclase and 20% for K-feldspar, Fig.6). Feldspars show various amounts of alteration (hydration). Poorly altered K-feldspars show the replacement of orthoclase by albite and small white micas, and formation of secondary porosity (Fig.7A). Highly altered feldspars are mostly replaced by white micas (Fig.7D). Most of the plagioclase has a high proportion of albite. Patches of quartz + micas are common mostly along crystal twins. Minor bulging recrystallisation is related to propagation of transgranular fractures in quartz and undulose extinction of quartz crystals is observed (Fig.7C, D).

Close to the top basement / sediment contact (inner damaged zone: < 20 m), the amount of feldspar (Fig.6) decreases (6% of orthoclase and no more albite), correlated with an increase of white micas (20%). Highly altered feldspars show extensive, up to complete

448 white mica replacement (Fig. 6D). The rock is clast-supported, dominated by quartz clasts.
449 Most of the clasts are derived from the gneiss, and the phyllosilicates are a by-product of
450 feldspar alteration leading to the formation of a white mica matrix (M1). White micas are
451 zoned, with an increase of Si and a decrease of Al toward their rims (Table 2). This results a
452 composition departing from the ideal composition of muscovite and being closer to that of
453 the illite-phengite group. Most of the white micas have a grain size below 50 µm,
454 corresponding to sericite (Eberl et al., 1987), but locally larger micas are observed (> 100
455 µm). Both quartz crystals inherited from the gneiss (where HT dynamic recrystallisation is
456 visible) and from the syn-kinematic veins (coarse grain blocky texture with no dynamic
457 recrystallisation of quartz and locally elongated to fibrous texture) commonly have a lobate
458 crystal border (Fig.7C) similar to a corrosive wear pattern and indicating quartz dissolution.
459 The inherited gneissosity is completely overprinted by brittle deformation (Fig.7C, D,
460 E). In the clast-rich areas, the clasts are rather angular, while in the areas with a higher
461 matrix-to-clast ratios, quartz grains are more rounded (Fig.7E). Most fractures and veins are
462 intergranular, but clusters of intragranular fractures are locally observed. These fractures are
463 branched with each other with an acute angle up to 45° (Fig.7E). Several events of quartz
464 fracturing are also highlighted by different generations of fluid inclusion trails in single quartz
465 grains, which have a fracture density of 28 μm^{-1}. Therefore, deformation is achieved by
466 fracturing associated with significant hydration and mineral neoformation (white micas and
467 quartz precipitation in the veins). These types of “chaotic fault rocks“ maintaining cohesion
468 during deformation are typical of cataclasites (Braathen et al., 2004). The grain size shows
469 fractal distribution with a fractal dimension between 1.38 and 1.5.
470 The fabrics described previously are later overprinted by larger transgranular veins
471 (Fig.7E). These veins are filled either with quartz or with iron sulphide or oxide. The quartz
472 veins (> 100 µm-thick) are themselves affected by fracturing and progressively reworked in
473 the cataclastic matrix corresponding to continuous vein formation throughout deformation.
474 The iron sulphide to oxide veins, which crosscut the quartz veins, are thinner (> 10 µm-thick).
475 Far from the contact, only sulphides are observed (6%), while closer to the contact only 1%
476 of pyrite is present, for 2% of rutile and 8% of iron oxide. No specific orientation of the clasts
477 nor the veins is visible.
478 Along the fault (core) zone, calcite-rich fractures are locally visible (Fig.7F). Calcite fills
479 fractures in the cataclasite with a jigsaw monogenic fabric. Cement is brown-coloured, with

480 locally preserved banded texture (2-3 mm). The cement is iron-rich, with a zoned iron
481 composition. The initial texture is composed of large dolomite rhombs with and small
482 ankerite rhombs and formation of calcite filling the space between the former minerals. It is
483 affected by static recrystallization leading to formation of equigranular twinned Mg- calcite.
484 Along the contact between the calcite-cemented fractures and the cataclasite, part of the
485 white micas and feldspars are also replaced by calcite forming patches. The jigsaw fabric
486 with important dilation points toward hydraulic fracturing resulting in breccias. Textural
487 relationships suggest that breccia formation corresponds to one of the latest deformation
488 events along the fault plane.
489
490 **3.3.3 Core zone**
491 The core zone is made of gouges, which are dark, fine-grained matrix-supported
492 rocks, which rework fragments of cataclasites (Fig.8A and B,). The rock shows the same
493 appearance microscopically as macroscopically, with the alternation of clast-rich and matrix-
494 rich layers. The high content in phyllosilicate points toward an indurated black gouge
495 following the definition of Braathen et al. (2004). In the clast-rich layers (at the microscale),
496 the quartz grains range from 1 mm to less than 10 µm in size. The grain size distribution
497 follows a power law with a fractal dimension β between 1.58 and 1.7 (Fig.9C). The shape of
498 the clasts is variable, ranging from angular to well-rounded (up to 0.9 circularity) with a
499 mean circularity of 0.59 (Fig.9F). Deformation of the clasts lead to the formation of σ-clasts
500 (Fig.8A), associated with small folded cataclasite clasts (Fig.8B). Preferential orientation of
501 the clasts (Fig.9E, e.g. Manatschal, 1999) highlights the foliation. The asymmetric clasts are
502 good kinematic markers. Asymmetric clasts are visible in the direction parallel to the N-S
503 stretching lineation indicating a top to the south sense of shear. The gouge matrix (M2)
504 corresponds mostly to illite-rich material less than 5 µm in size, with lower amounts of
505 quartz and pyrite (Fig.8C). Neoformed illite growing perpendicularly from the pyrite walls in
506 pressure shadows are also present. Small zircons (less than 50 µm) inherited from the gneiss
507 are affected by fracturing and minor dissolution at the micro-scale. Oxide-rich bands
508 represent 5% of the whole samples (2% of iron oxide and 2.7% of rutile) (Fig.8E). Most of the
509 pyrite was dissolved, leaving holes in the rock surrounded by quartz pressure shadows. Post-
510 kinematic mineralogical transformations are also observed. Only a small amount of pyrite is
511 preserved or weathered to jarosite. Coarser white micas (up to 100 µm long, XMs>0.7) are

visible in the gouge and the cataclasite clasts. They appear post-dating the gouge growing sometimes over the gouge foliation (Fig 8.D). Finally, micrometric hematite-filled fractures can locally be observed in the gouge, where they crosscut and thus postdate the foliation.

Dilation and vein formation also occurred in the core zone. Small (2 mm-thick), fractured quartz veins are visible in the matrix. Some veins crosscut the foliation and are affected by fracturing with millimetric offsets, while other veins are parallel to the foliation. Pressure shadows filled with fibrous quartz can have developed around quartz vein fragments. Besides, thin (< 100 µm-thick) iron oxide rich veins parallel to the foliation plane are present. A last vein generation corresponds to centimetre-thick veins visible at the macroscale, parallel to the gouge foliation (Fig.8E, Fig.9A and B). They are not observed in the adjacent cataclasites. The veins are filled by quartz and Ba-rich feldspar (hyalophane) (Fig.8E and F). The Ba content of hyalophane is around 11 to 15% wt, corresponding to a composition of 23% Celsian, 4% Albite and 71.9% orthoclase. The hyalophane crystals, which are euhedral, show no compositional zoning. They are partially replaced by quartz mainly along their cleavage (Fig. S7). On the border of the veins, hyalophane crystals are highly fractured, with reworking of some fragments in the gouge. An important amount of transgranular fractures affecting quartz and hyalophanes are also visible (fracture density of 18 μm^{-1}) with some corresponding to healed fractures with fluid inclusion trails.

More information on the processes occurring during the formation of gouge M2 from the cataclasite is obtained with quantitative compositional mapping by electron probe micro-analyser (EPMA), highlighting the behaviour of major elements and the textural evolution during deformation (Fig.10). Phase maps (Fig.10A) show quartz and feldspars grains in a white mica matrix. For the white micas, a reduction of the grain size is visible for white micas larger than 10 µm in the cataclasite and smaller than 10 µm in the gouge matrix M2 (Fig.10B). The progressive shearing of the cataclasite matrix M1 has an impact not only on the grain size but also on the composition of the micas (Fig.10B and C). Except for the K_2O and SiO_2 contents, which remain stable (10 wt%), and the Al_2O_3 that decreases, other major element contents increase between the cataclasite and the gouge matrix (Fig.10F). The increase is particularly important for TiO_2 as visible in the chemical map (Fig.10C), the chemical profile (Fig.10D) highlighting the absence of TiO_2 in the cataclasite and presence in the gouge matrix. Recalculation of structural formulas show a slight decrease of Al VI and Al IV between the cataclasite matrix and the gouge matrix (1.75 +/- 0.07 apfu (atom per

formula unit) to 1.67 +/- 0.04 apfu and 0.58 +/- 0.06 apfu to 0.55 +/- 0.040 apfu for Al VI and Al IV, respectively).. Detailed compositional analysis of the phyllosilicates from the gouge matrix (M2 (Fig.10E; Table 2) show departure from the Mu-Ce line (phengite). This indicates that Si-Al substitution is not achieved through a tschermak substitution ($Al^{IV}Al^{VI} \leftrightarrow Si^{IV}(Mg,Fe^{2+})^{VI}$) but through a pyrophyllite substitution ($Al^{IV}M^{I} \leftrightarrow Si^{IV}\square^{I}$) and illite substitution $Al^{VI}\square^{I} \leftrightarrow Mg^{VI}M^{I}$, leading to charge deficit and formation of illite (Meiller (2013)) with interfoliar charge between 0.8 and 0.9(Meiller (2013)).

4. Discussion

4.1. Conditions and mechanisms of deformation

4.1.1. Progressive deformation in retrograde conditions

Detailed petrographical and microstructural observations suggest that the studied rocks forming the top basement of the internal Mont Blanc Massif can be best interpreted as belonging to a fault zone. The fault rocks record the overprint of an initially high-temperature Variscan fabric in the gneissic basement, by a cataclastic deformation at much lower temperatures. In the gneiss, the observation of sub-grain rotation and grain boundary migration during dynamic recrystallisation of quartz grains points to temperatures of around 450 to 600°C during the formation of a first, primary foliation (Stipp et al., 2002). Such high temperature fabrics would correspond to depths of 15 to 20 km considering an average gradient of 20°C/km (determined using P-T date on skarns (Marshall et al., 1997). These depths are similar to those of emplacement of the lower part Mont-Blanc pluton at around 15 km (6 to 8 Kbar north Mont-Blanc massif; Marshall et al., 1997), suggesting that this Variscan fabric was acquired during the Carboniferous, before any significant exhumation. In the damage zone, this fabric is first overprinted by feldspar fracturing, minor quartz bulging recrystallisation and hydration (Fig.11A). The association of brittle behaviour of feldspars and minor plastic deformation of quartz is indicative of a deformation temperature of around 275°C to 300°C (Stipp et al., 2002), corresponding to a depth of about 7 km assuming a geothermal gradient of 40°C/km (derived from heat flow modeling during necking of the crust (Chenin et al., 2020)). This deformation was associated with significant hydration of the basement, as seen by widespread feldspar sericitization and chloritization of biotite (Fig.11A), still under lower greenschist facies metamorphic conditions. Toward the fault core zone, deformation is more intense and accompanied by an almost complete feldspar

replacement by muscovite and illite, and the disappearance of both biotite and chlorite. These metamorphic reactions occurred simultaneous to an increasing brittle overprint during which the host rock lost its initial HT fabric to become a clast supported cataclasite, with an increase of the phyllosilicate content toward the core zone. Cataclastic flow as observed here is found at depth ranging between 12 to 5 km (Sibson, 1986), which is in agreement with a decrease of the overburden during deformation and simultaneous exhumation. The progressive alteration of the rock during brittle deformation resulted in the localisation of deformation in phyllosilicate-rich zones, resulting in the matrix supported core zone (black gouge M2). The observation of rounded clasts of cataclasite in this gouge supports the interpretation that the gouge formed within a previously brittle deformed and altered basement. Petrographical and geochemical observations demonstrate that the gouge matrix was formed by progressive shearing of the cataclasite matrix, associated with a change in composition and grain comminution (Fig.11A). The decrease of Si in the white micas in the cataclasite and corresponding increase in the gouge is consistent with fluid-mediated diffusion of Si and Al across the fault zone and progressive enrichment in Si in the fine-grained gouge matrix, along with the neoformation of illite. The absence of crystal plastic recrystallisation of quartz during gouge formation indicates that frictional deformation was the dominant deformation mode. This restricts the temperature to below 275°C, which corresponds to the onset of plastic deformation (Stipp et al., 2002). Brittle behaviour is also visible through the high microfracture density of cataclasite grains, as well as through the significant grain comminution in the gouge. Indeed, the low fractal dimension (β = 1.3-1.7) calculated in the gouge is an illustration of this friction-dominant, scale independent process leading to grain size reduction. It is in the range of both generic and detachment gouges (Boulton et al., 2009), which have been shown to be commonly formed at levels shallower than 5 km depth (Sibson, 1986), where conditions for extensive clay formation are met (low T and low P) . Finally, transition from plastic/frictional deformation to pure frictional deformation and reworking of cataclasites in the gouge points to exhumation along a retrograde path as deformation proceeded. This exhumation of the basement reached the surface where formation of fissures filled with a crinoid mud affected the already tectonized basement and was sealed by the Grès Singuliers.

4.1.2 Strain softening due to phyllosilicate neoformation along brittle fault plane

Deformation at retrograde, fluid assisted alteration was associated with important phyllosilicate replacement and neoformation in the cataclasite and particularly in the gouge. It is thus likely that the phyllosilicates played a key role in the mechanical evolution and behaviour of the fault (e.g. Wintsch et al., 1995; Jefferies et al., 2006; Wibberley, 2005; Imber et al., 2008; Wallis et al., 2015). Indeed, from the proportion of illite to quartz (80% of clay) in the gouge M2, and using the experimental work on gouge friction of Tembe et al. (2010), the gouge can be estimated to have had a friction coefficient (μ) lower than 0.3 (Fig.11A), without considering the possible impact of fluid pressure in facilitating slip along the fault plane. Such a low-friction coefficient must be compared with that of gneissic rocks , which is expected to be >0.6 (Ikari et al., 2011). This behaviour is best explained by the neoformation of phyllosilicates, which led to significant strain-softening at the transition from a clast to matrix/phyllosilicate supported fabric, promoting, and facilitating slip along the fault plane. In clays, this frictional sliding is enhanced by the presence of interlayer water (when present) and a deficit in interlayer cations, leading to a low bonding of the octahedral and tetrahedral layer facilitating slip (Morrow et al., 2000). In addition to the phyllosilicates, the injection of gouge matrix (M2) into the cataclasites, both at macroscopic and microscopic scales, shows that the gouge locally behaved like a fluid. This is best explained by local fluid overpressure developing in the gouge during transient deformation events (e.g. Manatschal, 1999), likely associated with gouge compaction and pore reduction during shearing (e.g. Faulkner et al., 2018). However, several observations suggest that the mechanical behaviour of the fault gouge evolved from low- to high-friction. The last event affecting the gouge was the formation of quartz/ hyalophane veins emplaced parallel to the gouge foliation. Although the age of the veins is not well constrained, the brecciation of some veins and the presence of clasts of hyalophane in the gouge M2 and the cataclasite tends to indicate a syn-kinematic emplacement of these veins. At present-day the gouge is indurated, which is not compatible with a low friction coefficient. Induration may be explained by syn-kinematic quartz precipitation and presence of Si-rich pervasive fluid or recrystallisation of the illite matrix, possibly during Alpine orogenesis, as discussed later (Fig.11A). The fact that only cataclasites but no gouge clasts were found in the syn-rift sediments might point toward the second hypothesis. Nevertheless, adularia similar to the hyalophane variety from the veins are found commonly reworked in the Grès Singuliers (*Fig. S7*).

4.1.3 Fault-related basement hydration and fluid circulation

The mineral assemblages observed in the damaged basement and the fault rocks highlight the widespread presence of fluids during Jurassic deformation, while their chemical composition suggests the migration of some elements along the fault zone linked to fluid channelling. Indeed, several syn-kinematic metamorphic minerals are hydrated, mostly chlorite and white micas. Chlorite formed in replacement of biotite, which is a common reaction at greenschist facies conditions (Parry and Downey, 1982; Parneix et al., 1985). Chloritization was spatially restricted to the lowly deformed basement. The most important evidence of widespread hydration is the partial transformation of the K-feldspars to sericite and albite, followed by their complete replacement by white micas as deformation continued. The reaction was likely triggered by significant fracturing at both the macro and the microscale in the fault zone, increasing the permeability in the basement, facilitating fluid circulation (e.g., McCaig, 1988; Sibson, 2000; Manatschal et al., 2000; Wibberley and Shimamoto, 2003; Rossetti et al., 2010). Such effect is highlighted by important alteration around microfractures in the damaged zone, which indicates that fracturing at the micro scale increased the reactive surface available for fluid rock interaction (Plümper et al., 2017). In addition to phyllosilicates, several minerals precipitated in veins or locally in the fault gouge during deformation, such as iron rich sulphide/oxides, quartz, hyalophane, or rutile. Some minerals containing elements found in large concentrations in the protolith, such as quartz (Si) or iron sulphides/oxides (Fe), could have easily precipitated in a closed system, triggered by dissolution/precipitation mechanisms (e.g., Jefferies et al., 2006; McAleer et al., 2017). However, the presence of rutile and Ti-rich illite in the gouge matrix, or of hyalophane in veins, which are rich in Ti and Ba respectively, requires element transfer in a more open system. The systematic enrichment of the gouge matrix (M2) in Ti points to mobility of this element during gouge formation. Indeed, the gouge matrix was formed by shearing of the cataclasite matrix (M1), which is devoid of Ti. This indicates at least a minimum amount of Ti transfer in an open system at micro-scale, which is unexpected as this element is usually considered as immobile during fluid-rock interaction (Van Baalen, 1993; Rubin et al., 1993). In the same way, the presence of hyalophane mostly in late veins suggests the input of an external Ba-rich fluid. Such fluid mobility is not surprising, since faults can act as a conduit for fluids both in sedimentary basins and at crustal scales (McCaig,

1988; Manatschal et al., 2000; Sibson, 2000; Rossetti et al., 2010). However, fault permeability is extremely heterogenous (Wibberley and Shimamoto, 2003). In the damage zone (cataclasite), permeability reaches values of 10^{-14}-10^{-16}m^2, controlled mainly by mineral precipitation and dissolution, and by fracture development (Wibberley and Shimamoto, 2003). Dynamic permeability (crack and seal behaviour) related to local fluid overpressure build up along the fault during an interseismic cycle with fluid release during coseismic slip might have contributed to the overall permeability (Sibson, 1990; Sibson, 1992; Poulet et al., 2021). In the core zone (gouges), permeability is generally lower (10^{-17}-10^{-20}m^2) and anisotropy associated with the planar fabric of the phyllosilicates higher (Wibberley and Shimamoto, 2003; Kopf, 2001). In the studied fault, most of the veins observed are parallel to the foliation, where one could expect the highest permeability. It is thus likely that the gouge fabric had strong control of vein formation and related fluid circulation. Nevertheless, the origin of external fluids, such as a crustal source (dehydration of hydrated rocks) or the infiltration of water from the surface, remains to be determined. Ongoing mass-balance calculations should help to quantify more precisely the conditions of fluid mobility during fault-related deformation in the Col du Bonhomme area.

4.2 Is the Col du Bonhomme fault a Jurassic extensional detachment fault?

4.2.1. Sedimentological evidence for superficial exhumation along a detachment

An extensional detachment fault corresponds to an fault dipping gently (< 30°) and which can appear sub-horizontal at the surface (Boulton et al., 2009). Thus, syn-rift sediments can be deposited conformably above an exhumed fault surface, which is not possible for a thrust fault that results in burial. The extensional fault can either initiate at a low-angle, or alternatively initiate at a high-angle and rotate subsequently during exhumation at a low-angle near or at the surface. Isostatic uplift and low elastic strength in the footwall favour such a rotation (Axen and Hartley, 1997) and can lead to an important, kilometre-scale offset (Forsyth, 1992). Such faults are also referred to as rolling hinge faults (Wernicke and Axen, 1988; Lavier and Buck, 2002). They are usually associated with low frictional material along the fault plane. If the fault is exhumed under aerial or marine conditions, it can be submitted to erosion. In such a case, the fault surface can be eroded and becomes difficult to observe. The reworking of the fault rocks in the syn-exhumation sediments is a diagnostic feature of exhumed faults as observed for instance in the Basin and

Range (Yin and Dunn, 1992). Epin et al. (2017) defined diagnostic criteria to identify pre-Alpine, rift related detachment faults. A key observation is the presence of fault rocks at the top basement, overlaid by either pre-rift sediments along a tectonic contact, or by syn- to post-tectonic sediments in which case the contact is stratigraphic. Indeed, deposition of sediments above a fault plane is geometrically possible only above an extensional detachment fault, where the footwall is pulled out underneath its hanging wall. Both features are clearly observed in the Col du Bonhomme area.

First, remnants of pre-rift Triassic deposits are overlying cataclasites and gouges capping the basement along a tectonic contact. Similar examples have been described in the Pyrenees (Lagabrielle et al., 2010; Jammes et al., 2010) but also in the Alps, where pre-rift remnants are found over the exhumed crust in the necking, the distal and the exhumed mantle domains of the Adriatic margin (Mohn et al., 2010; Epin, 2017). These pre-rift blocks can range from tens of meters to kilometres. Many authors discussed the role of evaporites as potential decoupling levels controlling the preservation of supra-salt pre-rift cover sequence as allochthonous hanging-wall blocks over exhumed footwall (e.g., Jammes et al., 2010; Epin and Manatschal, 2018). In the case of the Col du Bonhomme, the anhydrite-bearing quartz locally found in recrystallized carbonates at the base of the pre-rift deposits suggests the former presence of evaporite levels below the dolomites, suggesting that they may have played a role during exhumation.

Second, the syn-rift deposits are sealing the exhumed fault surface, creating a stratigraphic contact. Field observations suggest that the oldest sediments deposited onto the detachment correspond to the crinoid-rich, brown-coloured breccias. The latter fills neptunian dykes that crosscut the basement cataclasites and gouges and is therefore necessarily younger than the fault rocks. A more recent age is also supported by reworking of the cataclasites and gouges in the breccias. A similar breccia, marked by the presence of lamellibranches, echinoderms and *Pentacrines* crinoids was also described by Landry (1976), 2 km southeast from the Col du Bonhomme (Crête des Gittes; 45°42’51.6’’/ 6°42’37.39’’). The first occurrence of crinoids in the Helvetic/Dauphinois domain began in the Hettangian, with massive deposition of crinoid-bearing limestones during the Sinemurian/Pliensbachian in the Grande Rousse, Belledonne, and Morcles Massifs (Roux et al., 1988; Loup, 1992; Barfety, 1985; Gillcrist, 1988; Chevalier, 2002; Epard, 1989). A similar, early syn-rift age for the breccia would be consistent with these studies, but also with the age of the overlying

Grès Singuliers which is assumed to be Sinemurian to Pliensbachian. Like the breccias, the Grès Singuliers are in stratigraphic contact with the tectonized basement, but also rework the diagnostic cataclasites. This not only indicates that the fault had to be exhumed at the surface, but also supports its pre-Alpine age.

Finally, in the Col du Bonhomme area, an unconformity of 10 to 20° is observed between the Grès Singuliers and the top basement surface. Assuming horizontal deposition, which is likely at least in the top Grès Singuliers, where no sedimentary structures indicative of deposition on a major slope were observed, a shallow, < 20° dip-angle between the sediments and the top basement can be reconstructed. All these observations are compatible with an interpretation in which the Mont Blanc massif is capped by a Jurassic low-angle, extensional detachment fault. The shallow dip at the surface may be due to the rotation of the fault due to isostatic uplift in response to fault activity (removal of the hanging wall; Lavier et al., 2000; Lavier and Buck, 2002). This uplift may have lead ultimately to the formation of the Mont-Blanc Island of Trümpy (1971) and Loup (1992), thus providing a source for the detrital syn-rift Grès Singuliers sandstones found around the Mont-Blanc Massif (Fig.11B; Ribes et al., 2020).

4.2.2. Interpretation of kinematic markers

Most of the Alpine deformation related to the emplacement of the Helvetic nappes in the Col du Bonhomme area was accommodated in the Aalenian shales overlying the Grès Singuliers, as already noted by Egli and Mancktelow (2013). This may explain why the pre-Alpine, rifted related cover-basement relationships at the Col du Bonhomme were not significantly affected by Alpine deformation. In the damage and core zones of the studied fault, a limited imprint is also supported by the lack of typical Alpine deformation recorded elsewhere in the Mont-Blanc basement, characterized by mylonitic shear zones. In addition, our kinematic measurements obtained in the pre-rift and in the basement (Fig.3G) are consistent with a normal fault having a top to the south sense of shear, which is hardly compatible with the Alpine directions measured in the area (E-W to NW-SE directions with top to the west or to the north-west sense of shear; Meyer, 2002; Egli and Mancktelow, 2013).

N-S directed syn-rift movement in the Mont-Blanc detachment differs from the NW-SE direction generally assumed for the extensional direction of the Alpine Tethys rift system

(Lemoine and Trümpy, 1987; Fig. 1). However, these local measurements cannot be directly compared to the direction of regional extension without considering the specificities of the Alpine Tethys European margin whose three-dimensional characteristics is poorly known. Such scale discrepancies may reflect kinematics complexities related to rift segmentation and inheritance. Many examples both from fossil and present-day margin, show the complex kinematics occurring along faults network, where locally sense of shear can be oblique to the direction of extension. The necking system along the Norwegian margin shows complex fault geometries at large scale (Osmundsen and Péron-Pinvidic, 2018), with fault orientations spreading over 90°, controlled mostly by inheritance (Muñoz-Barrera et al., 2020). More generally segmentation in extensional systems could be associated with the development of transfer zones where local stretching can be highly oblique to the direction of regional extension as demonstrated in metamorphic core complex (Le Pourhiet et al., 2014) and reproduced in rift segment boundaries (Le Pourhiet et al., 2017). Segmentation of the Alpine Tethys rift system by major NW-SE transfer zones have been postulated by many studies in particular between the Pelvoux and Argentera Massif and possibly between the Belledonne and Mont-Blanc Massif (e.g. Lemoine et al., 1989; Decarlis et al., 2017; Ribes et al., 2019a). It is also worth noting that recent studies in the Pyrenean rift have also emphasised that rift segment boundary is better preserved from subsequent underthrusting during orogeny than rift segment centers (Manatschal et al., 2021). For all these reasons, our N-S stretching measurements in the Mont-Blanc preserved detachment may suggest rift segmentation in the southern western border of the internal Mont-Blanc massif.

4.2.3. Mineralogical and geochemical evolution: Jurassic exhumation versus Alpine metamorphism

In addition to the arguments presented above, the exhumation of the footwall can be deduced from the retrograde path recorded by with the mineralogical assemblages of the fault rocks, which show a progressive decrease of temperature associated with the exhumation from sub-greenschist conditions to the surface. Most mineralogical assemblages identified are diagnostic of lower greenschist metamorphic conditions, with temperatures lower than ~300°C. These temperatures are very close to those reached during the Alpine metamorphic peak in the Col du Bonhomme (~330°C). These temperatures preclude the formation of biotite but are high enough to allow that of muscovite, raising the question of

the preservation of the parageneses related to Jurassic fault exhumation. Indeed, our observations show that such syn-kinematic parageneses correspond to extensive phyllosilicate formation, either muscovite in the cataclasite or illite in the gouge, and minor formation of rutile, quartz/hyalophane veins, iron sulphides and calcite. From these minerals, some could clearly have been altered or recrystallized during Alpine prograde metamorphism. This applies first to the white micas. It is not excluded that the present-day illite matrix of the gouge results from the prograde recrystallisation of a lower temperature clay. However, if illite formed during Jurassic extension, its preservation would not be surprising since illite-type white micas are stable until 350°C for the illite end-member, with complete disappearance of smectite above ca. 300°C (Velde, 1985; Merriman, 1999; Rosenberg, 2002; Meunier et al., 2004). In addition, illite whose presence is widespread in the Grès Singuliers and the Aalenian shales (Eltchaninoff and Triboulet, 1980), is known to form at least until 320°C (Eberl et al., 1987; Battaglia, 2004; Meunier et al., 2004). Then, the age of the white micas (sericite-type) observed in the pressure shadows of quartz fragments and sulphides is hard to assess, and an alpine age is possible. Minor muscovite static recrystallisation was also observed locally as overprinting the gouge matrix, possibly as a consequence of prograde metamorphism.

For some phases appearing the latest in the sequence (hyalophane-quartz veins, calcite), doubts remain as to a Jurassic or Alpine origin. In the gouge, the hyalophane-quartz veins are deformed and can be broken to clasts, which favors an early, Jurassic formation. The presence of detrital adularia in the Grès Singuliers clearly points in the same direction. However, the composition of the latter needs to be analysed in more detail to confirm a common origin with the hyalophane crystals of the veins. Finally, the Alpine overprint is likely responsible for the static recrystallisation of calcite in the basement, where the initial texture was almost completely lost and replaced by equigranular calcite.

To conclude, the contact between the tectonized top basement and the sediments is clearly pre-Alpine, and the Alpine metamorphic overprint seems mostly static with partial recrystallisation of low temperature minerals such as the gouge clay matrix and calcite.

4.3 Large scale implication of the Mont-Blanc detachment fault

The presence of a rift-related detachment fault in the Mont-Blanc Massif might have a variety of implications for its Alpine history. First, this study shows that major rift-related

structures can be preserved even in deformed parts of an orogen, in accordance with previous observations in the Alps (Barfety and Gidon, 1984; Lemoine and Trümpy, 1987; Manatschal, 1999; Cardello and Mancktelow, 2014; Epin and Manatschal, 2018; Pantet et al., 2020; Nibourel et al., 2021) and the Pyrenees (Izquierdo-Llavall et al., 2020; Espurt et al., 2019; Labaume and Teixell, 2020; Lescoutre and Manatschal, 2020). Indeed, the large-scale architecture of the Mont-Blanc massif proposed by Ribes et al. (2020) put the Mont-Blanc at the transition between the proximal and the distal domains of the former European margin, indicating a specific crustal architecture.

The thinning of the crust is highlighted by the increase of the accommodation space and the presence of exhumed mantle (Beltrando et al., 2012). According to the model of the H-Block (Fig. 11C; Lavier and Manatschal, 2006), thinning during the necking of the crust is accommodated by two conjugated faults located in the upper brittle crust and in the lower crust. The Mont-Blanc detachment fault could correspond to the upper crust detachment where the deformation is mostly (if not entirely) brittle. The lower crust conjugate fault might have been preserved as interpreted from the ECORS-CROP profile (Thouvenot et al., 1996; Mohn et al., 2014).

Preservation was probably better in the southern edge of the Mont-Blanc Massif, where the rift-related structures are oblique to the main thrust axis, and therefore likely transported passively. At present, the thrust nappes from the external part of the Mont-Blanc (former proximal domain) present polyharmonic folds (e.g., Morcles nappe; Ramsay, 1989; Epard, 1990), whereas in the internal part of the Mont-Blanc Massive, the thrust nappes are characterized by disharmonic folding (e.g., Wildhorn and Diableret nappes; Ramsay, 1989). Fold nappes in the external domains are generated by half-graben inversion as shown by field evidence (e.g., Bourg d'Oisan basin; Chevalier, 2002) or by numerical models (Bauville and Schmalholz, 2015; Kiss et al., 2020). The geometry of the disharmonic thrust nappes from the internal Mont-Blanc may thus be explained by the role of structural inheritance from the Mont-Blanc detachment fault, leading to a different Jurassic basin architecture and position of decollement level.

In addition, important hydration of the basement around the detachment level during Jurassic rifting, in part linked with an open fluid circulation, could have changed the rheological behaviour of the crust, by diminishing its strength (Wintsch et al., 1995), as postulated for example in the Axial zone of the Pyrenees by Bellahsen et al. (2019) and

Airaghi et al.(2020). Indeed, thin-skinned and thick-skinned fold thrust belts are controlled by thermal inheritance but also by structural (Mohn et al., 2014; Tavani et al., 2021) and chemical inheritance (Lacombe and Bellahsen, 2016). A rheologically weakened basement following fault-related hydration promotes thick-skin style of deformation during shortening, and could accommodate large amounts of deformation through a localised or diffused deformation zone, which is observed in the external crystalline massifs of the Alps (Bellahsen et al., 2014; Bellanger et al., 2015; Nibourel et al., 2021; Rosenberg et al., 2021). Finally, because of its potential role in both collision-related deformation and fluid flow during Alpine metamorphism, our study shows that the extent of Jurassic deformation and associated basement hydration clearly deserves further characterisation.

Conclusion

This work was focused on the field, petrographic, microstructural, and geochemical characterization of a tectonic surface recently discovered in the Col du Bonhomme area as part of the Mont-Blanc Massif, and previously described as a Jurassic detachment fault. The tectonic surface affects mostly the gneissic basement of the massif, which is heavily deformed into cataclasite above which Sinemurian to Pliensbachian sediments were deposited.

In detail, the cataclastic basement is increasingly deformed toward its top. Deformation was excusively the brittle field and associated with hydration of the basement, visible through the increase of phyllosilicate neoformation, which is likely responsible for the observed strain localisation. Overall, the transition from sub-greenschist brittle deformation to gouge formation with low-T clays points towards a retrograde path during fault activity, leading ultimately to exhumation to the surface, which is also supported by the reworking of clasts of fault-rocks in the overlying syn-rift sandstones. All these observations are fully consistent with an interpretation of the top basement as a Jurassic extensional detachment fault. They also suggest that important hydration of the basement and vein formation could be related to fluid circulation along the fault plane, although additional work is needed to confirm this interpretation.

Finally, the description of a pre-Alpine detachment fault in the Mont-Blanc Massif shows that preservation of such rift-related structures is possible in the External Crystalline

massifs despite significant Alpine deformation. It also raises the question of the role played by this structure during Alpine shortening. Nevertheless, this detachment also provides a field analogue for the necking domain of rifted margins where both the sedimentary cover and the tectonic structure of the basement are preserved.

Acknowledgements

This work benefited from the financial support of E2S-UPPA to the first author. We thank P. de Parseval for EPMA analysis, P-H Leloup and A. Mercier for joining us to the field excursion, J-L Epard, H. Masson, A. Pantet, C. Wibberley, E. Masini for fruitful discussions and J-M Kluska for help on the petrographical analysis of the samples. We thank N. Mancktelow and an anonymous reviewer as well as D. Grujic, guest editor, for their interesting comments that helped us improving the manuscript.

References

Airaghi, L., Bellahsen, N., Dubacq, B., Chew, D., Rosenberg, C., Janots, E., Waldner, M., Magnin, V., 2020. Pre-orogenic upper crustal softening by lower greenschist facies metamorphic reactions in granites of the central Pyrenees. Journal of Metamorphic Geology 38, 183–204.

Argand, E., 1916. Sur l'arc des Alpes occidentales. G. Bridel.

Axen, G.J., Hartley, J.M., 1997. Field tests of rolling hinges: Existence, mechanical types, and implications for extensional tectonics. Journal of Geophysical Research: Solid Earth 102, 20515–20537.

Barfety, J.C., 1985. Le Jurassique dauphinois entre Durance et Rhône: étude stratigraphique et géodynamique; évolution d'une portion de la marge nord téthysienne (Alpes occidentales françaises). Université Scientifique et Médicale de Grenoble.

Barfety, J.-C., Gidon, M., 1984. Un exemple de sédimentation sur un abrupt de faille fossile. Revue de Géologie Dynamique et de Géographie Physique 25, 267–276.

Battaglia, S., 2004. Variations in the chemical composition of illite from five geothermal fields: a possible geothermometer. Clay Minerals 39, 501–510.

Bauville, A., Schmalholz, S.M., 2015. Transition from thin- to thick-skinned tectonics and consequences for nappe formation: Numerical simulations and applications to the Helvetic nappe system, Switzerland. Tectonophysics 665, 101–117. https://doi.org/10.1016/j.tecto.2015.09.030

Bellahsen, N., Bayet, L., Denele, Y., Waldner, M., Airaghi, L., Rosenberg, C., Dubacq, B., Mouthereau, F., Bernet, M., Pik, R., Lahfid, A., Vacherat, A., 2019. Shortening of the axial zone, pyrenees: Shortening sequence, upper crustal mylonites and crustal strength. Tectonophysics 766, 433–452. https://doi.org/10.1016/j.tecto.2019.06.002

Bellahsen, N., Jolivet, L., Lacombe, O., Bellanger, M., Boutoux, A., Garcia, S., Mouthereau, F., Le Pourhiet, L., Gumiaux, C., 2012. Mechanisms of margin inversion in the external Western Alps: Implications for crustal rheology. Tectonophysics 560, 62–83.

Bellahsen, N., Mouthereau, F., Boutoux, A., Bellanger, M., Lacombe, O., Jolivet, L., Rolland, Y., 2014. Collision kinematics in the western external Alps. Tectonics 33, 1055–1088. https://doi.org/10.1002/2013TC003453

Bellanger, M., Augier, R., Bellahsen, N., Jolivet, L., Monié, P., Baudin, T., Beyssac, O., 2015. Shortening of the European Dauphinois margin (Oisans Massif, Western Alps): New insights from RSCM maximum temperature estimates and 40Ar/39Ar in situ dating. Journal of Geodynamics 83, 37–64. https://doi.org/10.1016/j.jog.2014.09.004

Beltrando, M., Frasca, G., Compagnoni, R., Vitale-Brovarone, A., 2012. The Valaisan controversy revisited: Multi-stage folding of a Mesozoic hyper-extended margin in the Petit St. Bernard pass area (Western Alps). Tectonophysics 579, 17–36. https://doi.org/10.1016/j.tecto.2012.02.010

Beyssac, O., Goffé, B., Chopin, C., Rouzaud, J.N., 2002. Raman spectra of carbonaceous material in metasediments: a new geothermometer. Journal of Metamorphic Geology 20, 859–871. https://doi.org/10.1046/j.1525-1314.2002.00408.x

Boulton, C., Davies, T., McSaveney, M., 2009. The frictional strength of granular fault gouge: application of theory to the mechanics of low-angle normal faults. Geological Society, London, Special Publications 321, 9. https://doi.org/10.1144/SP321.2

Bousquet, R., Goffé, B., Vidal, O., Oberhänsli, R., Patriat, M., 2002. The tectono-metamorphic history of the Valaisan domain from the Western to the Central Alps: New constraints on the evolution of the Alps. GSA Bulletin 114, 207–225. https://doi.org/10.1130/0016-7606(2002)114<0207:TTMHOT>2.0.CO;2

Bousquet, R., Oberhänsli, R., Goffé, B., Wiederkehr, M., Koller, F., Schmid, S.M., Schuster, R., Engi, M., Berger, A., Martinotti, G., 2008. Metamorphism of metasediments at the scale of an orogen: a key to the Tertiary geodynamic evolution of the Alps. Geological Society, London, Special Publications 298, 393–411.

Boutoux, A., Bellahsen, N., Nanni, U., Pik, R., Verlaguet, A., Rolland, Y., Lacombe, O., 2016. Thermal and structural evolution of the external Western Alps: Insights from (U–Th–Sm)/He thermochronology and RSCM thermometry in the Aiguilles Rouges/Mont Blanc massifs. Tectonophysics 683, 109–123.

Braathen, A., Osmundsen, P.T., Gabrielsen, R.H., 2004. Dynamic development of fault rocks in a crustal-scale detachment: An example from western Norway. Tectonics 23. https://doi.org/10.1029/2003TC001558

Bussy, F., Hernandez, J., Von Raumer, J., 2001. Bimodal magmatism as a consequence of the post-collisional readjustment of the thickened Variscan continental lithosphere (Aiguilles Rouges-Mont Blanc Massifs, Western Alps). Earth and Environmental Science Transactions of The Royal Society of Edinburgh, 91(1-2), 221-233.

Butler, R.W., 2017. Basement–cover tectonics, structural inheritance and deformation migration in the outer parts of orogenic belts: a view from the western Alps. Geological Society of America, Memoirs 213, 55–74.

Butler, R.W.H., 1989. The influence of pre-existing basin structure on thrust system evolution in the Western Alps. Geological Society, London, Special Publications 44, 105. https://doi.org/10.1144/GSL.SP.1989.044.01.07

Butler, R.W.H., 1986. Thrust tectonics, deep structure and crustal subduction in the Alps and Himalayas. Journal of the Geological Society 143, 857. https://doi.org/10.1144/gsjgs.143.6.0857

Cadenas, P., Fernández-Viejo, G., Pulgar, J.A., Tugend, J., Manatschal, G., Minshull, T.A., 2018. Constraints Imposed by Rift Inheritance on the Compressional Reactivation of a Hyperextended Margin: Mapping Rift Domains in the North Iberian Margin and in the Cantabrian Mountains. Tectonics 37, 758–785. https://doi.org/10.1002/2016TC004454

Cardello, G.L., Mancktelow, N.S., 2014. Cretaceous syn-sedimentary faulting in the Wildhorn Nappe (SW Switzerland). Swiss Journal of Geosciences 107, 223–250. https://doi.org/10.1007/s00015-014-0166-8

Cenki-Tok, B., Darling, J.R., Rolland, Y., Dhuime, B., Storey, C.D., 2014. Direct dating of mid-crustal shear zones with synkinematic allanite: new in situ U-Th-Pb geochronological approaches applied to the Mont Blanc massif. Terra Nova 26, 29–37. https://doi.org/10.1111/ter.12066

Chenin, P., Manatschal, G., Picazo, S., Müntener, O., Karner, G., Johnson, C., Ulrich, M., 2017. Influence of the architecture of magma-poor hyperextended rifted margins on orogens produced by the closure of narrow versus wide oceans. Geosphere 13, 559–576. https://doi.org/10.1130/GES01363.1

Chenin, P., Schmalholz, S.M., Manatschal, G., Duretz, T., 2020. Impact of crust–mantle mechanical coupling on the topographic and thermal evolutions during the necking phase of 'magma-poor' and 'sediment-starved' rift systems: A numerical modeling study. Tectonophysics 786, 228472. https://doi.org/10.1016/j.tecto.2020.228472

Chevalier, F., 2002. Vitesse et cyclicité de fonctionnement des failles normales de rift: implication sur le remplissage stratigraphique des bassins et sur les modalités d'extension d'une marge passive fossile: application au demi-graben liasique de Bourg-d'Oisans (Alpes occidentales, France). Université de Bourgogne.

Davis, G.H., Reynolds, S.J., Kluth, C.F., 2011. Structural geology of rocks and regions. John Wiley & Sons.

Debelmas, J., Lemoine, M., 1970. The western Alps: palaeogeography and structure. Earth Science Reviews 6, 221–256.

Decarlis, A., Beltrando, M., Manatschal, G., Ferrando, S., Carosi, R., 2017. Architecture of the Distal Piedmont-Ligurian Rifted Margin in NW Italy: Hints for a Flip of the Rift System Polarity. Tectonics 36, 2388–2406. https://doi.org/10.1002/2017TC004561

Decrausaz, T., Müntener, O., Manzotti, P., Lafay, R., Spandler, C., 2021. Fossil oceanic core complexes in the Alps. New field, geochemical and isotopic constraints from the Tethyan Aiguilles Rouges Ophiolite (Val d'Hérens, Western Alps, Switzerland). Swiss Journal of Geosciences 114, 1–27.

Demathieu, G., Weidmann, M., 1982. Les empreintes de pas de reptiles dans le Trias du Vieux Emosson. Eclogae Geologicae Helvetiae 721–757.

Dumont, T., Lemoine, M., Tricart, P., 1984. Pérennité de la sédimentation pélagique du Jurassique supérieur jusque dans le crétacé supérieur au-dessus de la croûte océanique téthysienne ligure: la

série supra-ophiolitique du lac des Cordes (zone piémontaise des Alpes occidentales au SE de Briançon). Comptes-rendus des séances de l'Académie des sciences. Série 2, Mécanique-physique, chimie, sciences de l'univers, sciences de la terre 299, 1069–1072.

Eberl, D.D., Srodon, J., Lee, M., Nadeau, P.H., Northrop, H.R., 1987. Sericite from the Silverton Caldera, Colorado; correlation among structure, composition, origin, and particle thickness. American Mineralogist 72, 914–934.

Egli, D., Mancktelow, N., 2013. The structural history of the Mont Blanc massif with regard to models for its recent exhumation. Swiss journal of geosciences 106, 469–489.

Eltchaninoff, C., 1980. Etude géologique entre Belledonne et Mont Blanc. La terminaison méridionale du massif du Mont Blanc et les terrains de son enveloppe. Université Paris VI, Paris.

Eltchaninoff, C., Triboulet, S., 1980. Étude Géologique entre Belledonne et Mont Blanc. Livre synthétique Travaux du Département de Géotectonique de l'Université Pierre et Marie Curie aParis 1–54.

Eltchaninoff-Lancelot, C., Triboulet, S., Doudoux, B., Fudral, S., Rampnoux, J.-P., Tardy, M., 1982. Stratigraphie et tectonique des unites delphino-helvetiques comprises entre Mont-Blanc et Belledonne (Savoie-Alpes occidentales); Implications regionales. Bulletin de la Société géologique de France 7, 817–830.

Elter, G., 1971. Schistes lustrés et ophiolites de la zone piémontaise entre Orco et Doire Baltée (Alpes Graies). Hypothèses sur l'origine des ophiolites. Géologie Alpine 47, 147–169.

Epard, J.L., 1990. La nappe de Morcles au sud-ouest du Mont-Blanc. Université de Lausanne.

Epard, J.-L., 1989. Triassic and Lias stratigraphy of the Dauphinoise zone between Belledonne, Aiguilles-Rouges and Mont Blanc. Bull. Soc. vaud. Sci. nat 79, 301–338.

Epard, J.-L., 1986. Le contact entre le socle du Mont-Blanc et la zone de Chamonix: implications tectoniques. Bull. Soc. vaud. Sci. nat 225–245.

Epin, M.-E., 2017. Evolution morpho-tectonique et magmatique polyphasée des marges ultra-distales pauvres en magma: la transition océan-continent fossile de l'Err et de la Platta (SE Suisse) et comparaison avec des analogues actuels. Strasbourg.

Epin, M.-E., Manatschal, G., 2018. Three-Dimensional Architecture, Structural Evolution, and Role of Inheritance Controlling Detachment Faulting at a Hyperextended Distal Margin: The Example of the Err Detachment System (SE Switzerland). Tectonics 37, 4494–4514. https://doi.org/10.1029/2018TC005125

Epin, M.-E., Manatschal, G., Amann, M., 2017. Defining diagnostic criteria to describe the role of rift inheritance in collisional orogens: the case of the Err-Platta nappes (Switzerland). Swiss Journal of Geosciences 110, 419–438.

Escher, A., Masson, H., Steck, A., 1993. Nappe geometry in the Western Swiss Alps. Journal of Structural Geology 15, 501–509. https://doi.org/10.1016/0191-8141(93)90144-Y

Espurt, N., Angrand, P., Teixell, A., Labaume, P., Ford, M., de Saint Blanquat, M., Chevrot, S., 2019. Crustal-scale balanced cross-section and restorations of the Central Pyrenean belt (Nestes-Cinca transect): Highlighting the structural control of Variscan belt and Permian-Mesozoic rift systems on mountain building. Tectonophysics 764, 25–45.

1053 Faulkner, D.R., Sanchez-Roa, C., Boulton, C., Den Hartog, S.A.M., 2018. Pore fluid pressure
1054 development in compacting fault gouge in theory, experiments, and nature. Journal of Geophysical
1055 Research: Solid Earth 123, 226–241.

1056 Ford, M., Duchêne, S., Gasquet, D., Vanderhaeghe, O., 2004. Coupling of internal and external
1057 orogenic processes in the western Alps, in: Réun. Sci. Terre.

1058 Forsyth, D.W., 1992. Finite extension and low-angle normal faulting. Geology 20, 27–30.
1059 https://doi.org/10.1130/0091-7613(1992)020<0027:FEALAN>2.3.CO;2

1060 Gillcrist, J.R., 1988. Mesozoic basin development and structural inversion in the external Franch Alps.
1061 Imperial college London.

1062 Glotzbach, C., Reinecker, J., Danišík, M., Rahn, M., Frisch, W., Spiegel, C., 2008. Neogene exhumation
1063 history of the Mont Blanc massif, western Alps. Tectonics 27. https://doi.org/10.1029/2008TC002257

1064 Guermani, A., Pennacchioni, G., 1998. Brittle precursors of plastic deformation in a granite: an
1065 example from the Mont Blanc massif (Helvetic, western Alps). Journal of Structural Geology 20, 135–
1066 148.

1067 Herwegh, M., Berger, A., Glotzbach, C., Wangenheim, C., Mock, S., Wehrens, P., Baumberger, R., Egli,
1068 D., Kissling, E., 2020. Late stages of continent-continent collision: Timing, kinematic evolution, and
1069 exhumation of the Northern rim (Aar Massif) of the Alps. Earth-science reviews 200, 102959.

1070 Herwegh, M., Pfiffner, O.A., 2005. Tectono-metamorphic evolution of a nappe stack: A case study of
1071 the Swiss Alps. Tectonophysics 404, 55–76. https://doi.org/10.1016/j.tecto.2005.05.002

1072 Holland, T.J.B., Powell, R., 2006. Mineral activity–composition relations and petrological calculations
1073 involving cation equipartition in multisite minerals: a logical inconsistency. Journal of Metamorphic
1074 Geology 24, 851–861.

1075 Ikari, M.J., Marone, C., Saffer, D.M., 2011. On the relation between fault strength and frictional
1076 stability. Geology 39, 83–86. https://doi.org/10.1130/G31416.1

1077 Imber, J., Holdsworth, R.E., Smith, S.A.F., Jefferies, S.P., Collettini, C., 2008. Frictional-viscous flow,
1078 seismicity and the geology of weak faults: a review and future directions. Geological Society, London,
1079 Special Publications 299, 151–173.

1080 Izquierdo-Llavall, E., Menant, A., Aubourg, C., Callot, J.-P., Hoareau, G., Camps, P., Péré, E., Lahfid, A.,
1081 2020. Preorogenic folds and syn-orogenic basement tilts in an inverted hyperextended margin: The
1082 Northern Pyrenees case study. Tectonics 39, e2019TC005719.

1083 Jammes, S., Huismans, R.S., 2012. Structural styles of mountain building: Controls of lithospheric
1084 rheologic stratification and extensional inheritance. Journal of Geophysical Research: Solid Earth 117.
1085 https://doi.org/10.1029/2012JB009376

1086 Jammes, S., Manatschal, G., Lavier, L., 2010. Interaction between prerift salt and detachment faulting
1087 in hyperextended rift systems: The example of the Parentis and Mauléon basins (Bay of Biscay and
1088 western Pyrenees). AAPG Bulletin 94, 957–975. https://doi.org/10.1306/12090909116

1089 Jefferies, S.P., Holdsworth, R.E., Shimamoto, T., Takagi, H., Lloyd, G.E., Spiers, C.J., 2006a. Origin and
1090 mechanical significance of foliated cataclastic rocks in the cores of crustal-scale faults: Examples from
1091 the Median Tectonic Line, Japan. Journal of Geophysical Research: Solid Earth 111.

Jefferies, S.P., Holdsworth, R.E., Wibberley, C.A.J., Shimamoto, T., Spiers, C.J., Niemeijer, A.R., Lloyd, G.E., 2006b. The nature and importance of phyllonite development in crustal-scale fault cores: an example from the Median Tectonic Line, Japan. Journal of Structural Geology 28, 220–235.

Jourdon, A., Le Pourhiet, L., Mouthereau, F., Masini, E., 2019. Role of rift maturity on the architecture and shortening distribution in mountain belts. Earth and Planetary Science Letters 512, 89–99. https://doi.org/10.1016/j.epsl.2019.01.057

Kiss, D., Duretz, T., Schmalholz, S.M., 2020. Tectonic inheritance controls nappe detachment, transport and stacking in the Helvetic nappe system, Switzerland: insights from thermomechanical simulations. Solid Earth 11, 287–305. https://doi.org/10.5194/se-11-287-2020

Kopf, A., 2001. Permeability variation across an active low-angle detachment fault, western Woodlark Basin (ODP Leg 180), and its implication for fault activation. Geological Society, London, Special Publications 186, 23–41.

Labaume, P., Teixell, A., 2020. Evolution of salt structures of the Pyrenean rift (Chaînons Béarnais, France): From hyper-extension to tectonic inversion. Tectonophysics 785, 228451.

Lacombe, O., Bellahsen, N., 2016. Thick-skinned tectonics and basement-involved fold–thrust belts: insights from selected Cenozoic orogens. Geological Magazine 153, 763–810. https://doi.org/10.1017/S0016756816000078

Lagabrielle, Y., 1987. Les ophiolites: marqueurs de l'histoire tectonique des domaines océaniques: le cas des Alpes franco-italiennes (Queyras, Piémont): comparaison avec les ophiolites d'Antalya (Turquie) et du Coast Range de Californie. Brest.

Lagabrielle, Y., Brovarone, A.V., Ildefonse, B., 2015. Fossil oceanic core complexes recognized in the blueschist metaophiolites of Western Alps and Corsica. Earth Science Reviews 141, 1–26.

Lagabrielle, Y., Labaume, P., de Saint Blanquat, M., 2010. Mantle exhumation, crustal denudation, and gravity tectonics during Cretaceous rifting in the Pyrenean realm (SW Europe): Insights from the geological setting of the lherzolite bodies. Tectonics 29.

Lanari, P., Vho, A., Bovay, T., Airaghi, L., Centrella, S., 2019. Quantitative compositional mapping of mineral phases by electron probe micro-analyser. Geological Society, London, Special Publications 478, 39–63.

Lanari, P., Vidal, O., De Andrade, V., Dubacq, B., Lewin, E., Grosch, E.G., Schwartz, S., 2014. XMapTools: A MATLAB©-based program for electron microprobe X-ray image processing and geothermobarometry. Computers & Geosciences 62, 227–240.

Landry, P., 1976. Contribution à l'étude géologique de la région de Roselend (Savoie). Univ. Grenoble, Grenoble.

Lavier, L.L., Buck, W.R., 2002. Half graben versus large-offset low-angle normal fault: Importance of keeping cool during normal faulting. Journal of Geophysical Research: Solid Earth 107, ETG 8-1. https://doi.org/10.1029/2001JB000513

Lavier, L.L., Buck, W.R., Poliakov, A.N.B., 2000. Factors controlling normal fault offset in an ideal brittle layer. Journal of Geophysical Research: Solid Earth 105, 23431–23442. https://doi.org/10.1029/2000JB900108

Lavier, L.L., Manatschal, G., 2006. A mechanism to thin the continental lithosphere at magma-poor margins. Nature 440, 324–328. https://doi.org/10.1038/nature04608

Le Pourhiet, L., Huet, B., Traore, N., 2014. Links between long-term and short-term rheology of the lithosphere: Insights from strike-slip fault modelling. Tectonophysics 631, 146–159.

Le Pourhiet, L., May, D.A., Huille, L., Watremez, L., Leroy, S., 2017. A genetic link between transform and hyper-extended margins. Earth and Planetary Science Letters 465, 184–192.

Leloup, P.-H., Arnaud, N., Sobel, E.R., Lacassin, R., 2005. Alpine thermal and structural evolution of the highest external crystalline massif: The Mont Blanc. Tectonics 24.

Lemoine, M., Bas, T., Arnaud-Vanneau, A., Arnaud, H., Dumont, T., Gidon, M., Bourbon, M., de Graciansky, P.-C., Rudkiewicz, J.-L., Megard-Galli, J., Tricart, P., 1986. The continental margin of the Mesozoic Tethys in the Western Alps. Marine and Petroleum Geology 3, 179–199. https://doi.org/10.1016/0264-8172(86)90044-9

Lemoine, M., Dardeau, G., Delpech, P.Y., Dumont, T., de Grasciansky, P.C., 1989. Extension Jurassique et failles transformantes jurassiques dans les Alpes occidentales. C. R. Acad. Sci. 1711–1716.

Lemoine, M., Gidon, M., Barfety, J.-C., 1981. Les massifs cristallins externes des Alpes occidentales: d'anciens blocs basculés nés au Lias lors du rifting téthysien. Comptes rendus des séances de l'Académie des sciences 2, 917–920.

Lemoine, M., Tricart, P., 1986. Les Schistes lustrés piémontais des Alpes occidentales: approche stratigraphique, structurale et sédimentologique. Eclogae Geologicae Helvetiae 79, 271–294.

Lemoine, M., Trümpy, R., 1987. Pre-oceanic rifting in the Alps. Tectonophysics 133, 305–320.

Lescoutre, R., Manatschal, G., 2020. Role of rift-inheritance and segmentation for orogenic evolution: example from the Pyrenean-Cantabrian systemRôle de l'héritage associé au rift et à sa segmentation pour l'évolution orogénique: exemple du système pyrénéo-cantabrique. Bulletin de la Société Géologique de France 191.

Loprieno, A., Bousquet, R., Bucher, S., Ceriani, S., Dalla Torre, F.H., Fügenschuh, B., Schmid, S.M., 2011. The Valais units in Savoy (France): a key area for understanding the palaeogeography and the tectonic evolution of the Western Alps. International Journal of Earth Sciences 100, 963–992. https://doi.org/10.1007/s00531-010-0595-1

Loup, B.F.R., 1992. Evolution de la partie septentrionale du domaine helvétique en Suisse occidentale au Trias et au Lias : contrôle par subsidence thermique et variations du niveau marin. Université de Genève, Genève.

Manatschal, G., 1999. Fluid- and reaction-assisted low-angle normal faulting: evidence from rift-related brittle fault rocks in the Alps (Err Nappe, eastern Switzerland). Journal of Structural Geology 21, 777–793. https://doi.org/10.1016/S0191-8141(99)00069-3

Manatschal, G., Chenin, P., Lescoutre, R., Miró, J., Cadenas, P., Saspiturry, N., Masini, E., Chevrot, S., Ford, M., Jolivet, L., 2021. The role of inheritance in forming rifts and rifted margins and building collisional orogens: a Biscay-Pyrenean perspective. BSGF-Earth Sciences Bulletin 192, 55.

Manatschal, G., Marquer, D., Früh-Green, G.L., 2000. Channelized fluid flow and mass transfer along a rift-related detachment fault (Eastern Alps, southeast Switzerland). GSA Bulletin 112, 21–33. https://doi.org/10.1130/0016-7606(2000)112<21:CFFAMT>2.0.CO;2

Manatschal, G., Sauter, D., Karpoff, A.M., Masini, E., Mohn, G., Lagabrielle, Y., 2011. The Chenaillet Ophiolite in the French/Italian Alps: An ancient analogue for an Oceanic Core Complex? Lithos 124, 169–184. https://doi.org/10.1016/j.lithos.2010.10.017

Marshall, D., Kirschner, D., Bussy, F., 1997. A Variscan pressure-temperature-time path for the NE Mont Blanc massif. Contributions to Mineralogy and Petrology 126, 416–428.

Masini, E., Manatschal, G., Tugend, J., Mohn, G., Flament, J.-M., 2014. The tectono-sedimentary evolution of a hyper-extended rift basin: the example of the Arzacq–Mauléon rift system (Western Pyrenees, SW France). International Journal of Earth Sciences 103, 1569–1596. https://doi.org/10.1007/s00531-014-1023-8

McAleer, R.J., Bish, D.L., Kunk, M.J., Sicard, K.R., Valley, P.M., Walsh, G.J., Wathen, B.A., Wintsch, R.P., 2017. Reaction softening by dissolution–precipitation creep in a retrograde greenschist facies ductile shear zone, New Hampshire, USA. Journal of Metamorphic Geology 35, 95–119.

McCaig, A.M., 1988. Deep fluid circulation in fault zones. Geology 16, 867–870.

Meiller, C., 2013. Etude cristallochimique de solutions solides de minéraux argileux. Impact de la déshydratation des smectites sur les surpressions dans les bassins sédimentaires. Université Pierre et Marie Curie-Paris VI.

Merriman, R.J., 1999. Patterns of low-grade metamorphism in metapelitic rocks. Low-grade metamorphism 60–107.

Meunier, A., Velde, B., Velde, B., 2004. Illite: Origins, evolution and metamorphism. Springer Science & Business Media.

Meyer, S., 2002. Etude géologique de la couverture mésozoïque para-autochtone du Mt-Blanc et des unités helvétiques au sud-ouest du Mt-Blanc. Institut de Géologie et Paléontologie, Université de Lausanne.

Mohn, G., Manatschal, G., Beltrando, M., Haupert, I., 2014a. The role of rift-inherited hyper-extension in Alpine-type orogens. Terra Nova 26, 347–353. https://doi.org/10.1111/ter.12104

Mohn, G., Manatschal, G., Beltrando, M., Masini, E., Kusznir, N., 2012. Necking of continental crust in magma-poor rifted margins: Evidence from the fossil Alpine Tethys margins. Tectonics 31. https://doi.org/10.1029/2011TC002961

Mohn, G., Manatschal, G., Masini, E., Müntener, O., 2011. Rift-related inheritance in orogens: a case study from the Austroalpine nappes in Central Alps (SE-Switzerland and N-Italy). International Journal of Earth Sciences 100, 937–961. https://doi.org/10.1007/s00531-010-0630-2

Monzawa, N., Otsuki, K., 2003. Comminution and fluidization of granular fault materials: implications for fault slip behavior. Tectonophysics 367, 127–143. https://doi.org/10.1016/S0040-1951(03)00133-1

Morrow, C.A., Moore, D.E., Lockner, D.A., 2000. The effect of mineral bond strength and adsorbed water on fault gouge frictional strength. Geophysical Research Letters 27, 815–818. https://doi.org/10.1029/1999GL008401

Muñoz-Barrera, J.M., Rotevatn, A., Gawthorpe, R.L., Henstra, G.A., Kristensen, T.B., 2020. The role of structural inheritance in the development of high-displacement crustal faults in the necking domain

of rifted margins: The Klakk Fault Complex, Frøya High, offshore mid-Norway. Journal of Structural Geology 140, 104163.

Nibourel, L., Berger, A., Egli, D., Heuberger, S., Herwegh, M., 2021. Structural and thermal evolution of the eastern Aar Massif: insights from structural field work and Raman thermometry. Swiss journal of geosciences 114, 1–43.

Osmundsen, P.T., Péron-Pinvidic, G., 2018. Crustal-Scale Fault Interaction at Rifted Margins and the Formation of Domain-Bounding Breakaway Complexes: Insights From Offshore Norway. Tectonics 37, 935–964. https://doi.org/10.1002/2017TC004792

Otsuki, K., 1998. An empirical evolution law of fractal size frequency of fault population and its similarity law. Geophysical Research Letters 25, 671–674. https://doi.org/10.1029/98GL00380

Pantet, A., Epard, J.-L., Masson, H., 2020. Mimicking Alpine thrusts by passive deformation of synsedimentary normal faults: a record of the Jurassic extension of the European margin (Mont Fort nappe, Pennine Alps). Swiss Journal of Geosciences 113, 13. https://doi.org/10.1186/s00015-020-00366-2

Parneix, J.C., Beaufort, D., Dudoignon, P., Meunier, A., 1985. Biotite chloritization process in hydrothermally altered granites. Chemical Geology 51, 89–101.

Parry, W.T., Downey, L.M., 1982. Geochemistry of Hydrothermal Chlorite Replacing Igneous Biotite. Clays and Clay Minerals 30, 81–90. https://doi.org/10.1346/CCMN.1982.0300201

Plümper, O., Botan, A., Los, C., Liu, Y., Malthe-Sørenssen, A., Jamtveit, B., 2017. Fluid-driven metamorphism of the continental crust governed by nanoscale fluid flow. Nature Geoscience 10, 685–690. https://doi.org/10.1038/ngeo3009

Poulet, T., Lesueur, M., Kelka, U., 2021. Dynamic modelling of overprinted low-permeability fault cores and surrounding damage zones as lower dimensional interfaces for multiphysics simulations. Computers & Geosciences 150, 104719.

Ramsay, J.G., 1989. Fold and fault geometry in the western Helvetic nappes of Switzerland and France and its implication for the evolution of the arc of the western Alps. Geological Society, London, Special Publications 45, 33. https://doi.org/10.1144/GSL.SP.1989.045.01.02

Rasband, W.S., 1997. ImageJ. Bethesda, MD.

Ribes, C., Ghienne, J.-F., Manatschal, G., Dall'Asta, N., Stockli, D.F., Galster, F., Gillard, M., Karner, G.D., 2020. The Grès Singuliers of the Mont Blanc region (France and Switzerland): stratigraphic response to rifting and crustal necking in the Alpine Tethys. International Journal of Earth Sciences 109, 2325–2352. https://doi.org/10.1007/s00531-020-01902-z

Ribes, C., Ghienne, J.-F., Manatschal, G., Decarlis, A., Karner, G.D., Figueredo, P.H., Johnson, C.A., 2019a. Long-lived mega fault-scarps and related breccias at distal rifted margins: insights from present-day and fossil analogues. Journal of the Geological Society 176, 801. https://doi.org/10.1144/jgs2018-181

Ribes, C., Manatschal, G., Ghienne, J.-F., Karner, G.D., Johnson, C.A., Figueredo, P.H., Incerpi, N., Epin, M.-E., 2019b. The syn-rift stratigraphic record across a fossil hyper-extended rifted margin: the example of the northwestern Adriatic margin exposed in the Central Alps. International Journal of Earth Sciences 108, 2071–2095.

Ribes, C., Petri, B., Ghienne, J.-F., Manatschal, G., Galster, F., Karner, G.D., Figueredo, P.H., Johnson, C.A., Karpoff, A.-M., 2019c. Tectono-sedimentary evolution of a fossil ocean-continent transition: Tasna nappe, central Alps (SE Switzerland). GSA Bulletin. https://doi.org/10.1130/B35310.1

Rolland, Y., Cox, S., Boullier, A.-M., Pennacchioni, G., Mancktelow, N., 2003. Rare earth and trace element mobility in mid-crustal shear zones: insights from the Mont Blanc Massif (Western Alps). Earth and Planetary Science Letters 214, 203–219. https://doi.org/10.1016/S0012-821X(03)00372-8

Rolland, Y., Rossi, M., Cox, S.F., Corsini, M., Mancktelow, N., Pennacchioni, G., Fornari, M., Boullier, A.-M., 2008. 40Ar/39Ar dating of synkinematic white mica: insights from fluid-rock reaction in low-grade shear zones (Mont Blanc Massif) and constraints on timing of deformation in the NW external Alps. Geological Society, London, Special Publications 299, 293–315.

Rosenbaum, G., Lister, G.S., 2005. The Western Alps from the Jurassic to Oligocene: spatio-temporal constraints and evolutionary reconstructions. Earth-Science Reviews 69, 281–306.

Rosenberg, C.L., Bellahsen, N., Rabaute, A., Girault, J.B., 2021. Distribution, style, amount of collisional shortening, and their link to Barrovian metamorphism in the European Alps. Earth-Science Reviews 103774. https://doi.org/10.1016/j.earscirev.2021.103774

Rosenberg, P.E., 2002. The nature, formation, and stability of end-member illite: A hypothesis. American Mineralogist 87, 103–107.

Rossetti, F., Aldega, L., Tecce, F., Balsamo, F., Billi, A., Brilli, M., 2010. Fluid flow within the damage zone of the Boccheggiano extensional fault (Larderello–Travale geothermal field, central Italy): structures, alteration and implications for hydrothermal mineralization in extensional settings. Geological Magazine 148, 558–579. https://doi.org/10.1017/S001675681000097X

Roux, M., Bourseau, J.-P., Bas, T., Dumont, T., de Graciansky, P.-C., Lemoine, M., Rudkiewicz, J.-L., 1988. Bathymetric evolution of the Tethyan margin in the western Alps (data from stalked crinoids): a reappraisal of eustatism problems during the Jurassic. Bulletin de la Société géologique de France, série 8, 633–41.

Rubin, J.N., Henry, C.D., Price, J.G., 1993. The mobility of zirconium and other “immobile” elements during hydrothermal alteration. Chemical Geology 110, 29–47. https://doi.org/10.1016/0009-2541(93)90246-F

Schmid, S.M., Fügenschuh, B., Kissling, E., Schuster, R., 2004. Tectonic map and overall architecture of the Alpine orogen. Eclogae Geologicae Helvetiae 97, 93–117.

Sibson, R.H., 2000. Fluid involvement in normal faulting. Journal of Geodynamics 29, 469–499.

Sibson, R.H., 1992. Implications of fault-valve behaviour for rupture nucleation and recurrence. Tectonophysics 211, 283–293. https://doi.org/10.1016/0040-1951(92)90065-E

Sibson, R.H., 1990. Conditions for fault-valve behaviour. Geological Society, London, Special Publications 54, 15–28.

Sibson, R.H., 1986. Earthquakes and Rock Deformation in Crustal Fault Zones. Annu. Rev. Earth Planet. Sci. 14, 149–175. https://doi.org/10.1146/annurev.ea.14.050186.001053

Stampfli, G.M., Hochard, C., 2009. Plate tectonics of the Alpine realm. Geological Society, London, Special Publications 327, 89. https://doi.org/10.1144/SP327.6

Stipp, M., StuÈnitz, H., Heilbronner, R., Schmid, S.M., 2002. The eastern Tonale fault zone: a 'natural laboratory'for crystal plastic deformation of quartz over a temperature range from 250 to 700 C. Journal of structural geology 24, 1861–1884.

Tavani, S., Granado, P., Corradetti, A., Camanni, G., Vignaroli, G., Manatschal, G., Mazzoli, S., Muñoz, J.A., Parente, M., 2021. Rift inheritance controls the switch from thin-to thick-skinned thrusting and basal décollement re-localization at the subduction-to-collision transition. GSA Bulletin.

Tembe, S., Lockner, D.A., Wong, T.-F., 2010. Effect of clay content and mineralogy on frictional sliding behavior of simulated gouges: Binary and ternary mixtures of quartz, illite, and montmorillonite. Journal of Geophysical Research: Solid Earth 115. https://doi.org/10.1029/2009JB006383

Thouvenot, F., Senechal, G., Truffert, C., Guellec, S., 1996. Comparison between two techniques of line-drawing migration (ray-tracing and common tangent method). Mémoires-Société Géologique de France, 53–60.

Tricart, P., De Graciansky, P., Lemoine, M., 2000. De l'océan à la chaîne de montagnes: tectonique des plaques dans les Alpes. Gordon and Breach.

Trümpy, R., 1971. Sur le Jurassique de la zone Helvétique en Suisse. Annales of the Geological Institute of Hungary 54, 370–382.

Trumpy, R., 1951. Le Lias de la Nappe de Bex (Préalpes internes) dans la Basse Gryonne. Bull. Soc. vaud. Sci. nat 161–182.

Van Baalen, M.R., 1993. Titanium mobility in metamorphic systems: a review. Chemical Geology 110, 233–249. https://doi.org/10.1016/0009-2541(93)90256-I

Velde, B., 1985. Clay minerals.

Wallis, D., Lloyd, G.E., Phillips, R.J., Parsons, A.J., Walshaw, R.D., 2015. Low effective fault strength due to frictional-viscous flow in phyllonites, Karakoram Fault Zone, NW India. Journal of Structural Geology 77, 45–61. https://doi.org/10.1016/j.jsg.2015.05.010

Wernicke, B., Axen, G.J., 1988. On the role of isostasy in the evolution of normal fault systems. Geology 16, 848–851. https://doi.org/10.1130/0091-7613(1988)016<0848:OTROII>2.3.CO;2

Wibberley, C.A., Shimamoto, T., 2003. Internal structure and permeability of major strike-slip fault zones: the Median Tectonic Line in Mie Prefecture, Southwest Japan. Journal of Structural Geology 25, 59–78.

Wibberley, C.A.J., 2005. Initiation of basement thrust detachments by fault-zone reaction weakening. Geological Society, London, Special Publications 245, 347. https://doi.org/10.1144/GSL.SP.2005.245.01.17

Wilson, J.T., 1966. Did the Atlantic Close and then Re-Open? Nature 211, 676–681. https://doi.org/10.1038/211676a0

Wilson, R.W., Houseman, G.A., Buiter, S.J.H., McCaffrey, K.J.W., Doré, A.G., 2019. Fifty years of the Wilson Cycle concept in plate tectonics: an overview. Geological Society, London, Special Publications 470, 1. https://doi.org/10.1144/SP470-2019-58

Wintsch, R.P., Christoffersen, R., Kronenberg, A.K., 1995. Fluid-rock reaction weakening of fault zones. Journal of Geophysical Research: Solid Earth 100, 13021–13032.

Wojdyr, M., 2010. Fityk: a general-purpose peak fitting program. Journal of Applied Crystallography 43, 1126–1128.

Yin, A., Dunn, J.F., 1992. Structural and stratigraphic development of the Whipple-Chemehuevi detachment fault system, southeastern California: Implications for the geometrical evolution of domal and basinal low-angle normal faults. Geological Society of America Bulletin 104, 659–674.

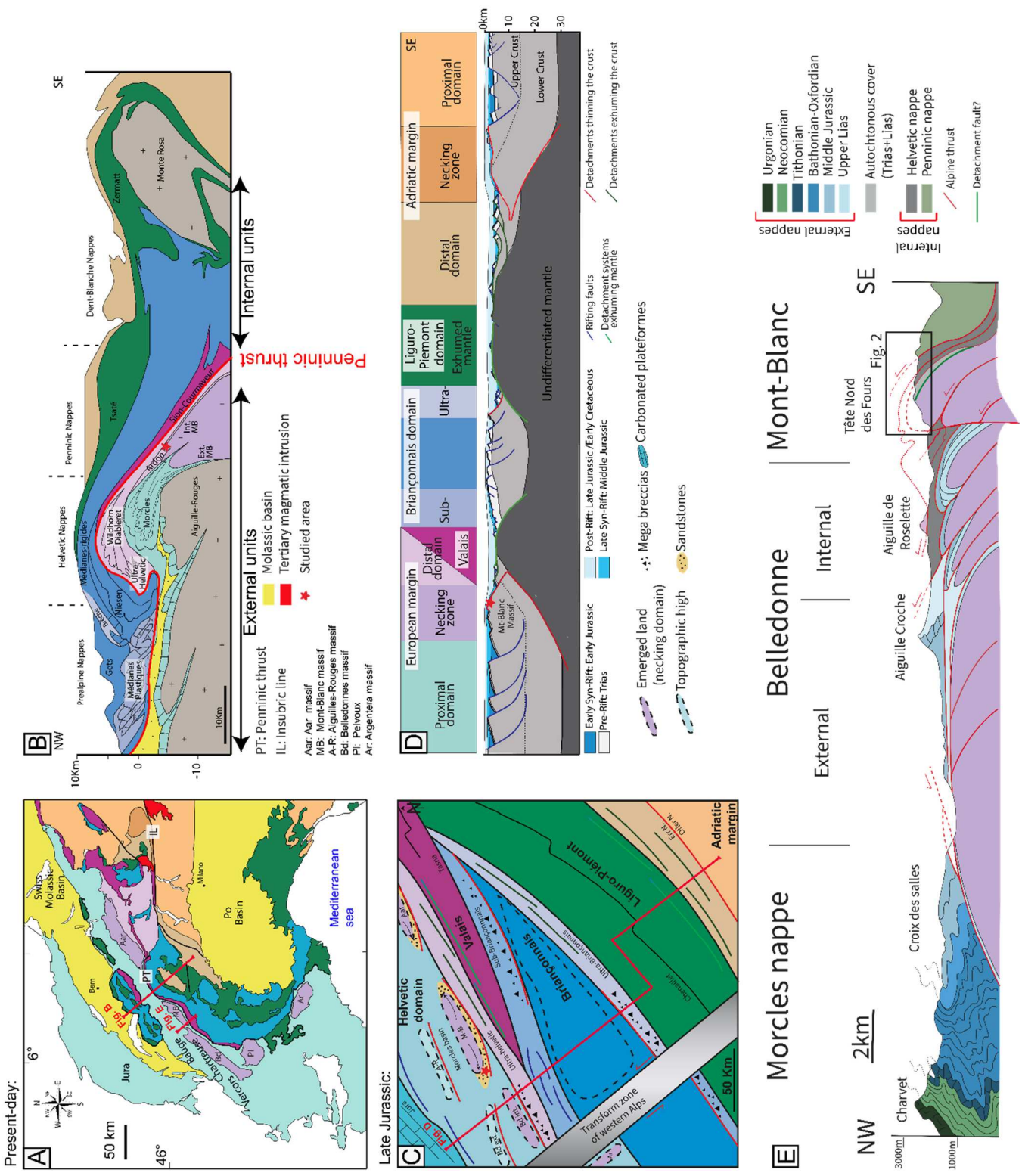

Fig1: A- Tectonic map of the Alps showing the different Alpine tectonic units. Note the presence of the External Crystalline Massifs (ECM) at the transition between the internal and external domains (modified from Mohn et al. (2010); Schmid et al.(2004)). The colour code similar to D (except molassic basins in yellow and Tertiary intrusions in red) highlights the paleogeographic position of the different Alpine units. B- Section across the Western Alps (for location see Fig. 1A; modified from Escher et al.(1993a)). Colour code similar to D. C- Paleogeographic map of the Alpine realm during the late Jurassic (modified from Ribes et al., 2019a). Sandstones (Ribes et al., 2020) and breccias (Ribes et al., 2019b) related to tectonic activity are also represented. Faults in blue correspond to normal faults associated with stretching, the fault in red

corresponds to necking fault thinning the crust, and faults in green correspond to faults exhuming the crust and the mantle. D-Restored section of the Alpine Tethys during the Late Jurassic (Mohn et al., 2010). E- NW-SE directed cross section across the transition zone between the Belledonne and Mont-Blanc Massif (Southern Mont-Blanc massif, modified from Eltchaninoff-Lancelot et al. (1982)). The Penninic and Helvetic nappes thrusted above the ECM were later deformed by basement deformation leading to the formation of a large antiformal fold. The area of interest corresponds to the basement anticline pinched between the Helvetic nappes to the south and the Roselette nappe to the north.

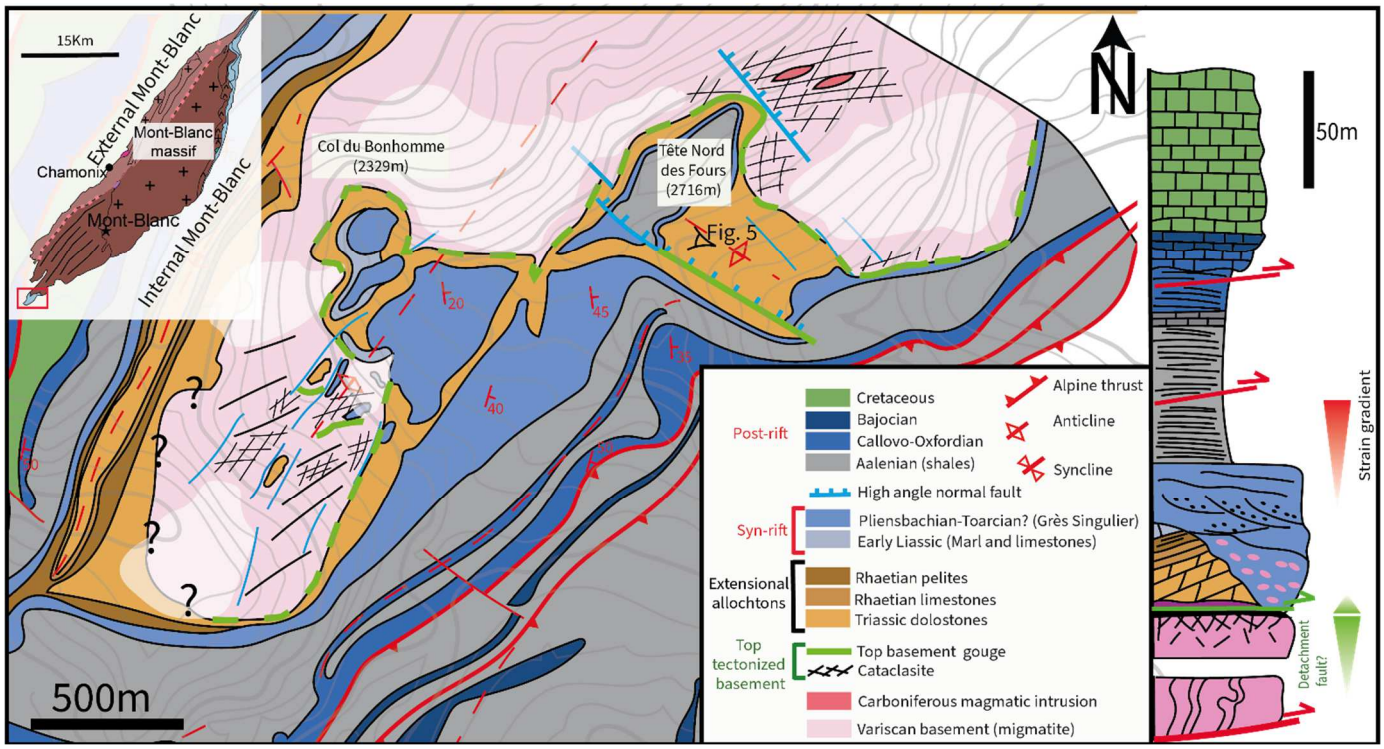

Fig2:-Map of the Col du Bonhomme area (see location on map in the upper left corner, modified from Meyer, (2002)) showing the southern edge of the Mont-Blanc Massif. The tectonic contact described by Ribes et al.(2020) is highlighted by the presence of cataclasite and gouge at the transition between the basement and the sediment. Numerous NE-SW and NW-SE Jurassic faults also offset the top basement tectonic contact. The section on the right shows the simplified stratigraphy from the top basement to the Cretaceous with the location of the main decollement levels in the area in the Aalenian and Oxfordian schists.

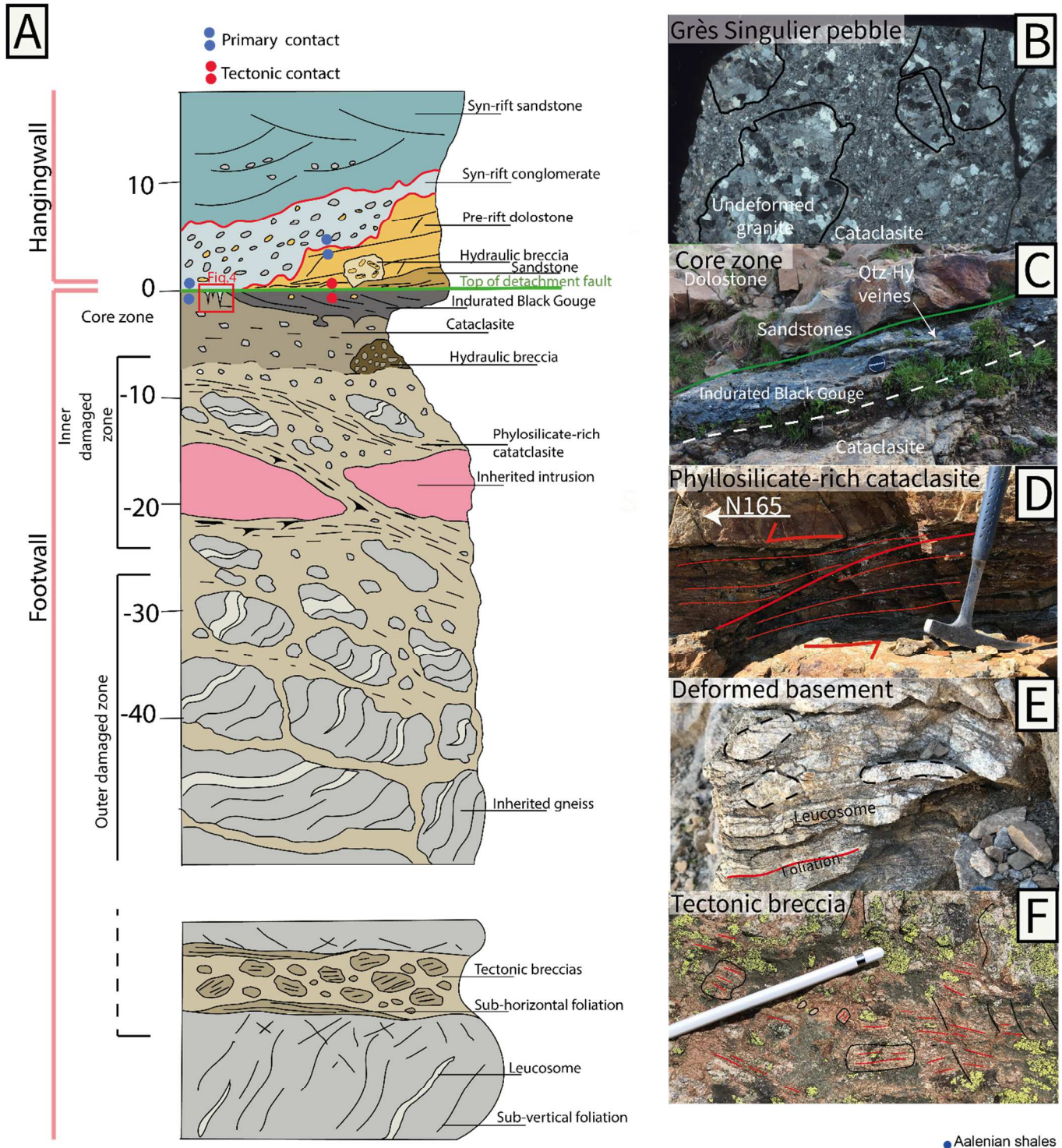
A
Primary contact
Tectonic contact
Hangingwall
Footwall
10
0
-10
-20
-30
-40
Core zone
Inner damaged zone
Outer damaged zone
Fig.4
Syn-rift sandstone
Syn-rift conglomerate
Pre-rift dolostone
Hydraulic breccia
Sandstone
Top of detachment fault
Indurated Black Gouge
Cataclasite
Hydraulic breccia
Phylosilicate-rich catatclasite
Inherited intrusion
Inherited gneiss
Tectonic breccias
Sub-horizontal foliation
Leucosome
Sub-vertical foliation
Grès Singulier pebble
B
Undeformed granite
Cataclasite
Core zone
C
Dolostone
Qtz-Hy veines
Sandstones
Indurated Black Gouge
Cataclasite
Phyllosilicate-rich cataclasite
D
N165
Deformed basement
E
Leucosome
Foliation
Tectonic breccia
F
G
Bedding and basement foliation
S0 Grès Singuliers
S0 Pre-rift
Variscan foliation
Sub-horizontal foliation
Sub-vertical foliation
Limb1
Limb2
Rolling hinge fold axis
Fold axis
Fault plane
Limb1
High angle normal fault
Limb2
Fold axis
Detachment fault
Lineation
Aalenian shales
Grès Singuliers
Pre-rift
Gouge
Cataclasite
Alpine deformation

Fig3: A-Schematic section of the top basement/sediment contact showing a strain gradient toward the top of the basement. A local loss of the initial rock texture is visible associated with an increase of alteration and brittle overprint. A sharp contact separates the basement and the sedimentary cover. Pre-rift sediments are separated from the basement by a tectonic contact with deformation visible at the base. The Grès Singuliers are lying above both the pre-rift and the basement in a stratigraphic contact. B-Clast of cataclasite reworked in the Grès Singuliers (45°43'46.41''N/ 6°43'47.96''E). C- The top basement is composed of cataclasite and locally black indurated gouge (45°43'39.51''N/6°42'40.25''E). D- Phyllosilicate-rich cataclasite giving an NNE-SSSW top to the south sense of shear in the damaged zone (45°46'13.36''N/6°43'46.17''E). E-Cataclased basement with sub-horizontal Variscan foliation is still discernible in the damaged zone (45°44'11.21N/6°43'46.85''E). F- Sub-horizontal mylonites affected by brittle deformation. G-Measures of bedding, fault plane orientations (high angle-normal faults and orientations of the top basement tectonic contact) and stretching lineations from the basement and the cover (projected on Schmidt stereograms, lower hemisphere). Note the NE-SW orientation of the basement fold affecting the basement and the cover (limb 1 and 2).

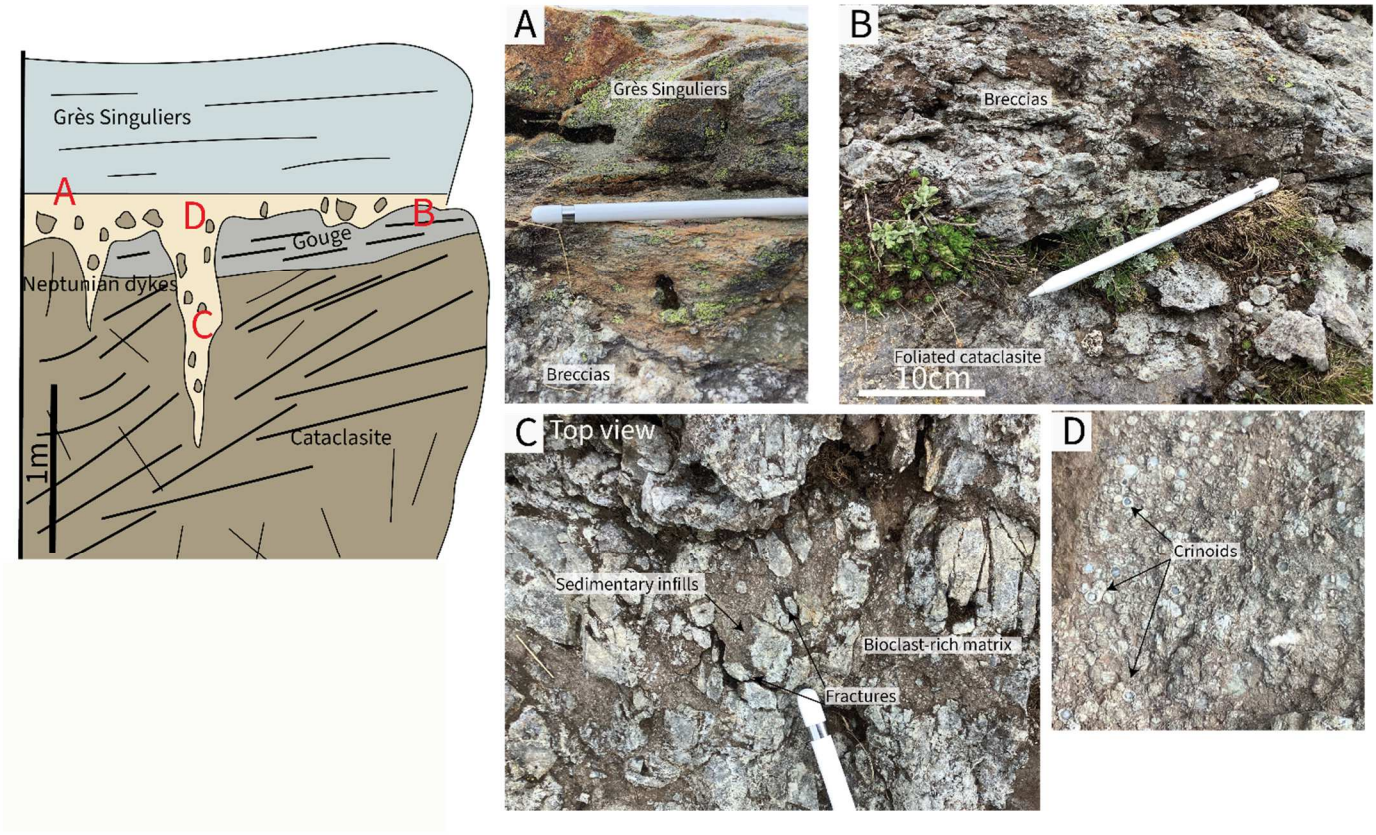

Fig4: Section of the top basement with sediment infill interpreted as neptunian dykes (45°43'39.6''N/6°42'46''E). The position of the pictures is indicated in the section. A- Contact between the top basement and the Grès Singuliers. B-Profile view of foliated cataclasite overlaid by fractured basement. The fractures are filled with a brownish matrix. C- Upper view of the fractured basement with sedimentary infill. The infill is composed of quartz grains and bioclasts fragments in a brownish matrix. D-View of the bioclasts from the matrix corresponding mainly to crinoids.

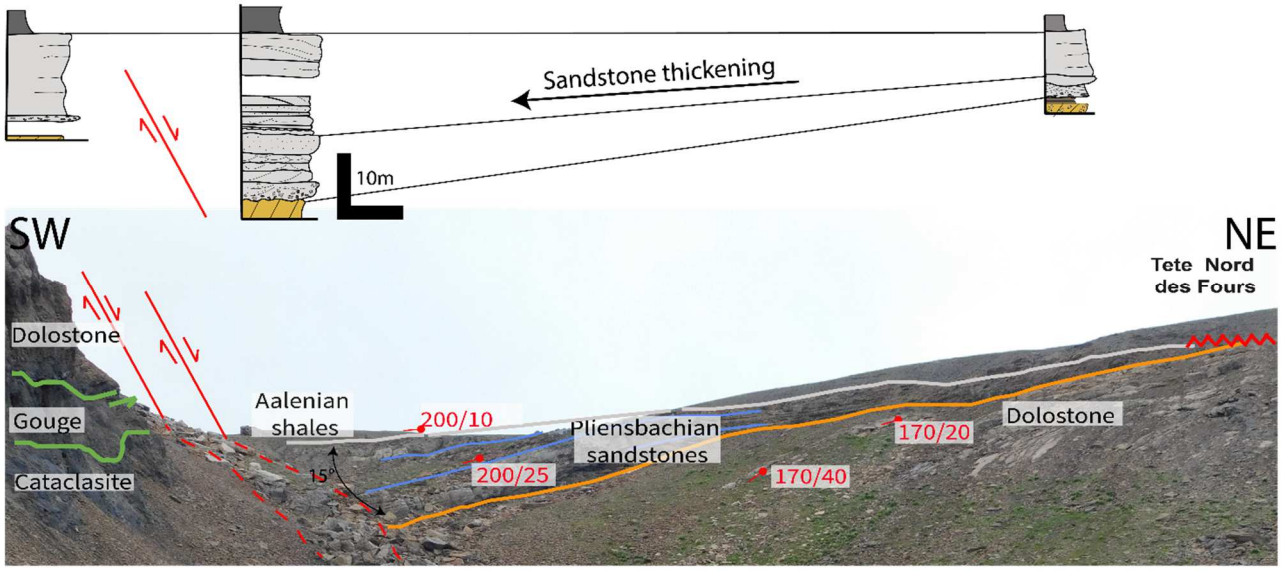

Fig5: High-angle normal fault offsetting the top basement tectonic contact about 30 m (45°43'53.45''/6°43'51.70''). A sedimentary wedge with thickening of sandstones toward the fault is observed in the Grès Singuliers (15°), indicating a likely Pliensbachian/Toarcian age for the fault.

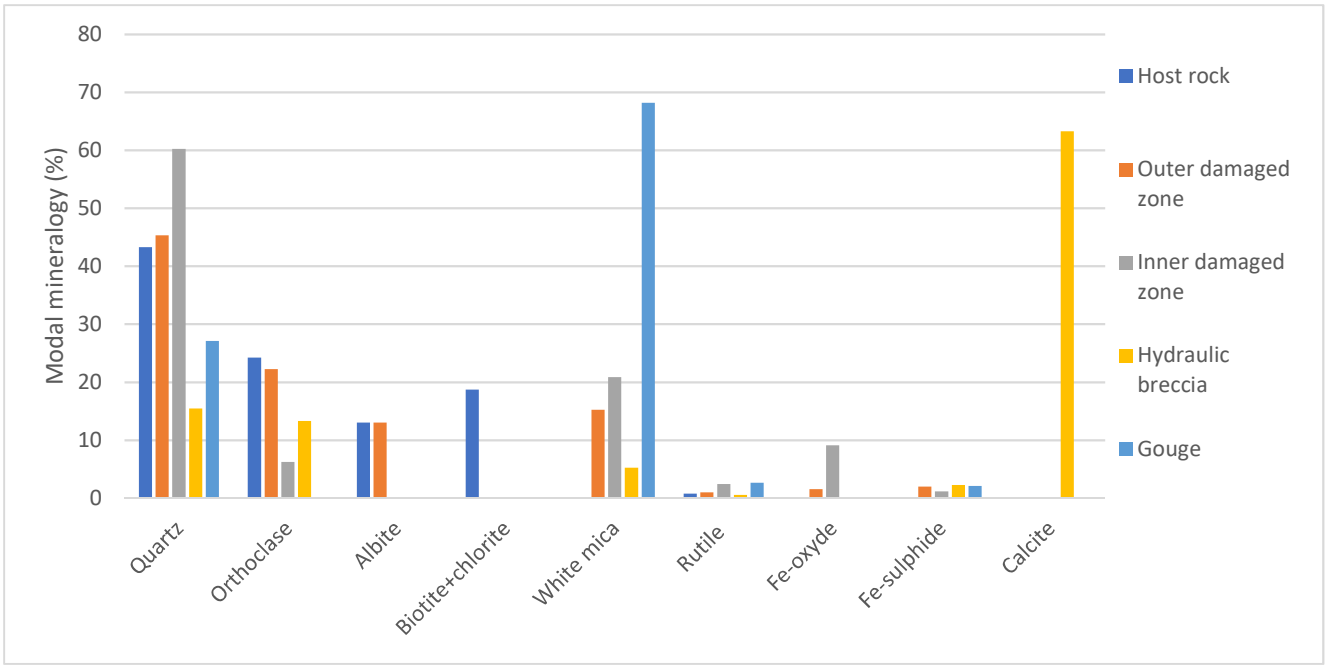

Fig6: Modal composition for some of the different fault rocks found in the Col du Bonhomme area.

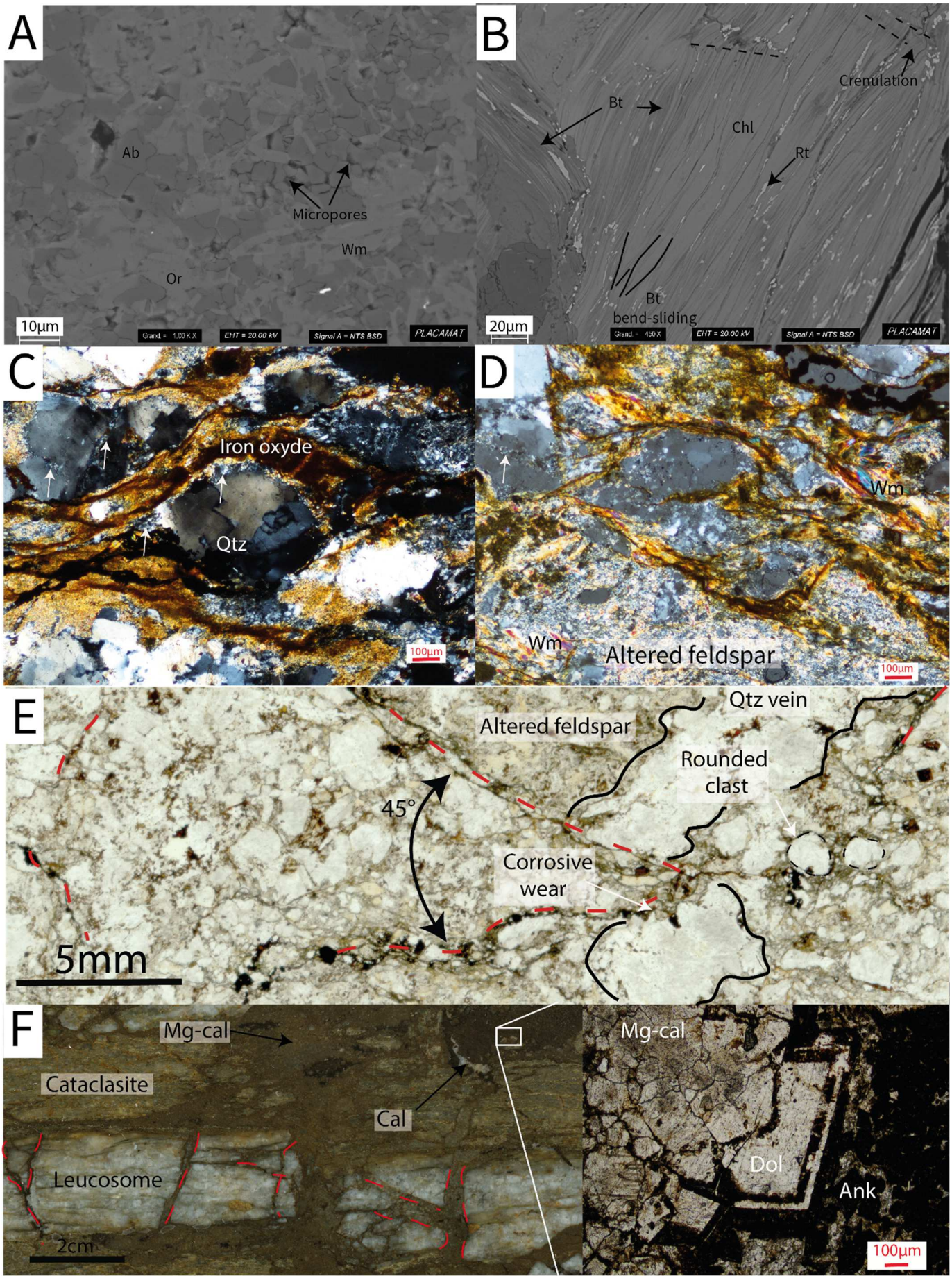
A
Ab
Micropores
Wm
Or
10µm
B
Crenulation
Bt
Chl
Rt
Bt
bend-sliding
20µm
C
Iron oxyde
Qtz
100µm
D
Wm
Wm
Altered feldspar
100µm
E
Altered feldspar
Qtz vein
Rounded
clast
45°
Corrosive
wear
5mm
F
Mg-cal
Cataclasite
Cal
Leucosome
2cm
Mg-cal
Dol
Ank
100µm

Fig7: A-Lowly altered orthoclase (Or) showing albite (Ab) and white mica (Wm) replacement with creation of microporosity (Scanning Electron microscope- Back Scattered Electron SEM-BSE). B- SEM-BSE image of the alteration of biotite (Bt) to chlorite (Chl) with formation of rutile (Rt). Note the alteration along the cleavage and on the borders of the crystals. Minor deformation such as crenulation is visible in the biotite and chlorite assemblages. C- Closer view of the cataclasite where numerous fractures filled with oxides are observed. Quartz (Qtz) exhibits fractures and minor plastic recrystallisation (bulging, white arrow) associated with undulose extinction (optical photomicrograph, crossed polarized light (XPL)) D- Cataclasite showing important feldspar alteration, with the formation of white micas associated with fracturing and oxides. Minor plastic recrystallization by bulging is visible in the prolongation of fractures (white arrow) (optical photomicrograph, XPL). E- Cataclasite showing fragmentation of the protolith, along with important fracturing of quartz and important hydration of feldspar (optical photomicrograph, plane polarized light (PPL)). Only few remnants of K-feldspars are observed. Partial dissolution of quartz with corrosive wear is clearly visible. Highly deformed quartz veins are observed in the cataclastic matrix, and oxide-rich fractures overprint the cataclasite. F- Hydraulic breccia with calcite cement (left: optical photographs of polished slab; right: XPL photomicrographs). The leucosomes are only affected by perpendicular fractures. The gneiss is affected by stronger alteration and deformation. The rock is overprinted by brecciation and subsequent dolomite (Dol) and ankerite (Ank) formation replaced by later by Mg-calcite (Mg-cal).

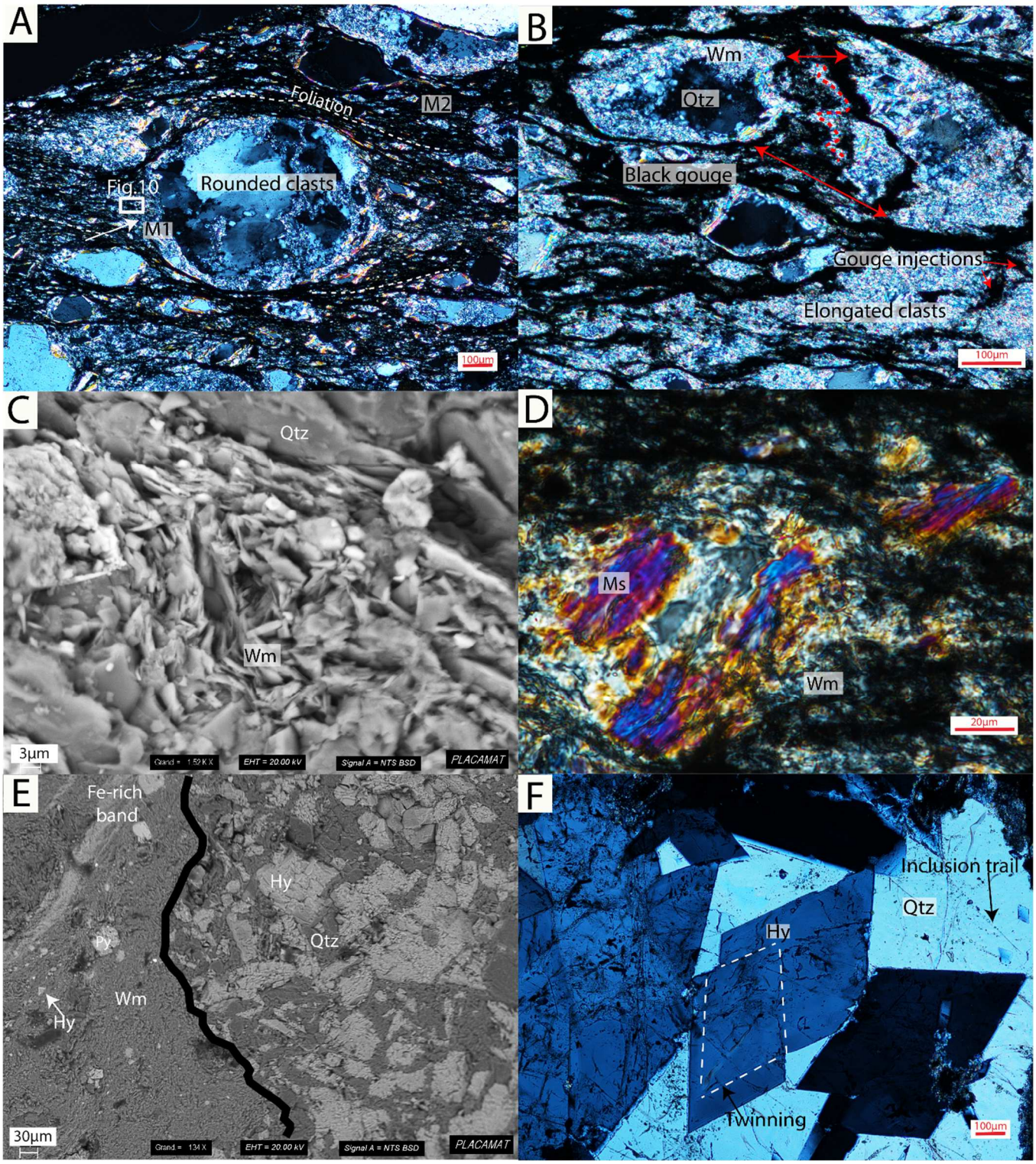

Fig 8: A-Microphotograph of the gouge showing a rounded clast embedded in the black matrix. The foliation is highlighted by the elongated clasts. The white arrow points at the cataclastic matrix (M1) of the clast progressively sheared and incorporated into the gouge matrix M2 (XPL). B- Microphotograph of the gouge matrix M1 with clasts of cataclasite

showing the progressive shearing (red arrows) and transformation into ultra-fine-grained black matrix M2 (XPL). C- Closer view of the black matrix of the gouge (M2) showing small illite minerals (around 5 µm), small quartz fragments (less than 10 µm) and pyrite (SEM-BSE, unpolished sample) D-Muscovite overgrowth over illite in the gouge (XPL). E- Irregular border between a hyalophane-bearing vein and the gouge. The latter is composed of small Fe-rich bands surrounded by illite-rich matrix. Clasts of hyalophane (Hy) are also observed in the gouge (SEM-BSE). F-Microphotograph of hyalophane and quartz in veins affected by important fracturing. The feldspars show important twinning of the crystals (XPL).

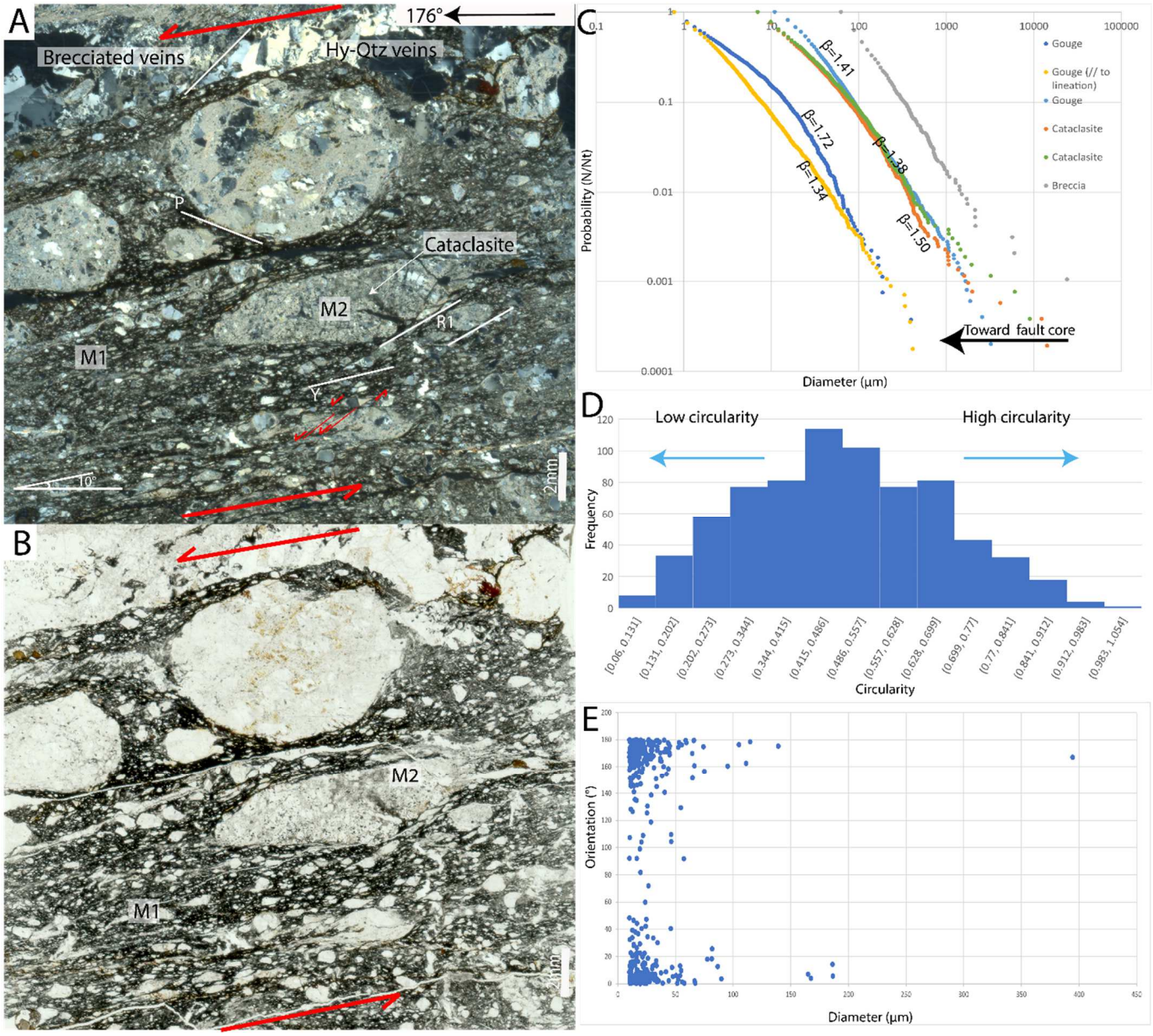

Fig 9: A and B- Microphotograph (XPL and PPL) of the black gouge reworking cataclasite fragments. The elongation of the clasts marks the foliation. Note the reworked clasts of cataclasite in the gouge matrix. C-Example of grain size repartition in gouge and cataclasite samples as obtained from image treatment. All the samples show a fractal dimension between 1.3 and 1.7. Note the progressive grain size diminution toward fault core. D-Grain size circularity of the gouge from image treatment showing a wide range of shapes, from angular to well rounded. E- Grain orientation versus grain size, showing a preferential orientation defining the foliation.

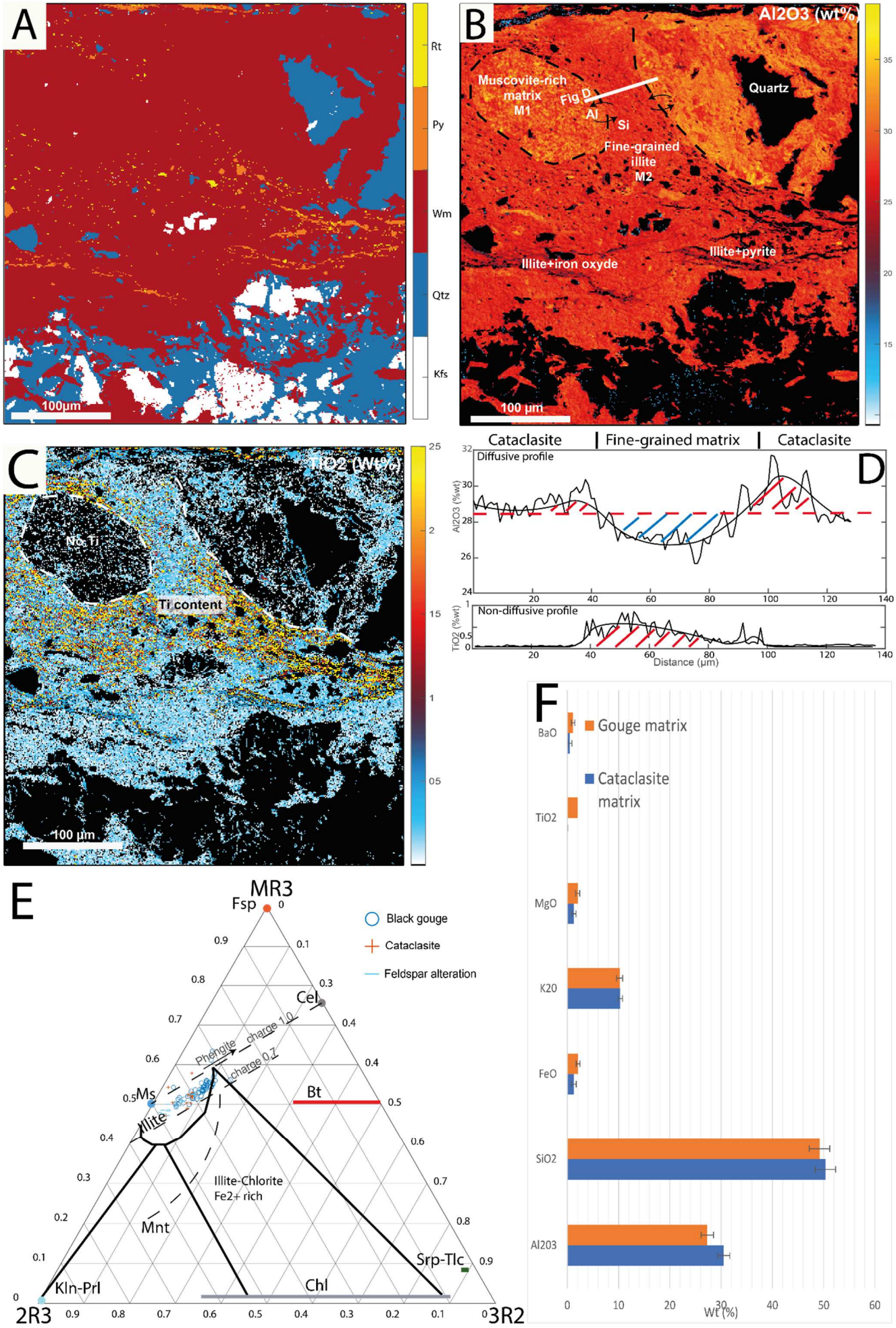
A
Rt
Py
Wm
Qtz
Kfs
100µm
B
Al2O3 (wt%)
Muscovite-rich matrix M1
Fig D
Al
Si
Quartz
Fine-grained illite M2
Illite+iron oxyde
Illite+pyrite
100 µm
C
TiO2 (Wt%)
No Ti
Ti content
100 µm
Cataclasite
Fine-grained matrix
Cataclasite
D
Diffusive profile
Al2O3 (%wt)
Non-diffusive profile
TiO2 (%wt)
Distance (µm)
E
MR3
Fsp
Black gouge
Cataclasite
Feldspar alteration
Cel
Phengite charge 1.0
charge 0.7
Ms
Bt
Illite
Illite-Chlorite Fe2+ rich
Mnt
Srp-Tlc
Kln-Prl
Chl
2R3
3R2
F
Gouge matrix
Cataclasite matrix
BaO
TiO2
MgO
K20
FeO
SiO2
Al203
Wt (%)

Fig10: A- Phase map from gouge microprobe mapping (Rt=rutile, Py=Pyrite, Wm=White micas, Qtz=Quartz, Kfs=K-feldspars). B and C - Microprobe maps of Al_2O_3 (B) and TiO_2 (C) showing distinct composition for the Wm phase. This highlights the different composition of the clasts of cataclasite (M1) and fine-grained gouge matrix (M2). The transition from the cataclasite matrix M1 to the gouge matrix M2 shows a loss of Al. Ti is absent from the cataclasite but hosted by rutile in the gouge. D- Profile across the micrometric fault zone for Al2O3 and TiO2. The Al2O3 content has a diffusive profile, contrary to TiO2 (in red, the zone of gain and in blue the zone of loss). E- Ternary plot of the composition of phyllosilicates from the gouge. MR3 = Na+K+2Ca, 2R3 = (Al+FeIII-MR3)/2, 3R2 = (Mg+ FeII)/3 (Velde, 1985). Ms = Muscovite, Cel = Celadonite, Fsp = Feldspars, Kln = Kaolinite, Prl = Pyrophyllite, Chl = Chlorite, Bt = Biotite, Srp = Serpentinite, Tlc = Talc, Mnt = Montmorillonite. F- Average microprobe composition of the cataclasite matrix and gouge matrix (muscovite to illite) for the major elements.

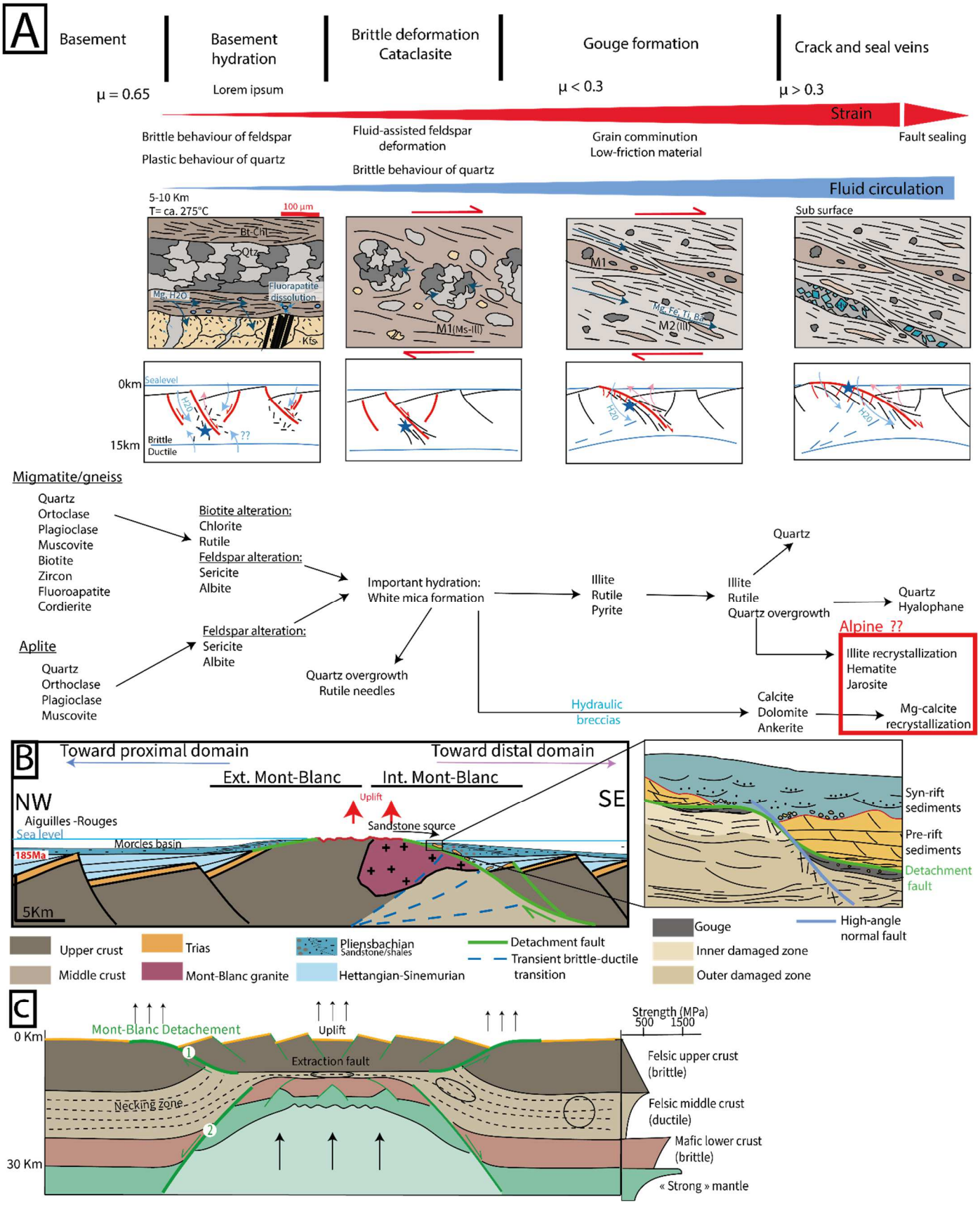

Fig11: A- Sketch summarizing the evolution of the fault rocks during exhumation following a retrograde path and a progressive localisation of the deformation in phyllosilicate rich layers (gouge) toward the surface. This is associated with the petrological evolution observed in the Col du Bonhomme from the gneiss to the matrix-supported gouge. The evolution

of frictional coefficient is indicated. B- Pliensbachian cross section of Mont-Blanc showing the crustal architecture and sedimentary infill associated to Mont-Blanc detachment fault (modified from Ribes et al. (2020)). Uplift related to the detachment fault led to local erosion and sandstones formation around the massif about the exhumed surface. C- The H-block model for the necking of the crust showing to conjugated fault system in the upper brittle crust and in the lower crust leading to crustal thinning (modified from Mohn et al. (2012)).

Sample	*Location*	*Lithologies*	*Coordinates*	*Nb of spectra*	*R1*	*R2*	*T (°C)*	*1σ SD (°C)*	*95% SD (°C)*	*95% SEM (°C)*
CB20-40	Col des Fours	Aalenian shales	45°45'52.06''/6°44'9.68''	21	2.47	0.71	322	6.52	18	3.96
CB20-41	Col des Fours	Aalenian shales	45°45'51.37''/6°44'7.22''	18	1.73	0.68	336	7.2	25.6	6.02
MB1c	Col des Fours	Liassic Carbonate	45°45'55.10''/6°44'16.06''	16	2.53	0.71	325	7.4	22.5	5.62

Table 1: Results of RSCM thermometry in the Col du Bonhomme area. SD=Standard deviation, SEM= Standard error of the mean, 95% confidence interval.

Samples	*CB20-10*										*5a*					*5c*	
	Protolith										Cataclasite		Gouge				
	Chl	**Chl**	**Bi**		**Fsp**	**Fsp**			**Fap**		**Wm**	**Wm**	**Wm**	**Wm**		**Hy**	**Hy**
SiO2	24.89	24.88	35.28	**SiO2**	65.13	63.98	68.63	**CaO**	52.18	**SiO2**	51.82	49.14	48.25	51.09	**SiO2**	54.49	53.50
TiO2	0.00	0.00	3.35	**TiO2**	0.00	0.00	0.23	**MnO**	0.98	**TiO2**	0.10	0.47	2.87	0.27	**TiO2**	0.00	0.00
Al2O3	20.81	20.68	19.15	**Al2O3**	19.09	18.46	18.88	**FeO**	0.57	**Al2O3**	25.95	26.66	29.73	27.92	**Al2O3**	20.17	20.17
Cr2O3	0.00	0.00	0.00	**Cr2O3**	0.00	0.00	0	**F**	2.67	**Cr2O3**	0.00	0.00	0.00	0.00	**Cr2O3**	0.00	0.00
Fe2O3	0.00	0.00	0.00	**Fe2O3**	0.00	0.00	0.17	**MgO**	0.03	**Fe2O3**	0.00	0.25	0.00	0.00	**Fe2O3**	0.00	0.00
FeO	28.30	27.51	17.96	**FeO**	0.00	0.00	0	**Cl**	0.07	**FeO**	2.56	1.76	1.47	1.99	**FeO**	0.04	0.04
MnO	0.44	0.44	0.35	**MnO**	0.00	0.00	0	**P2O5**	43.02	**MnO**	0.03	0.09	0.00	0.00	**MnO**	0.04	0.01
MgO	11.56	11.66	8.45	**MgO**	0.00	0.01	0.02	**SrO**	0.01	**MgO**	3.71	3.64	1.95	3.16	**MgO**	0.00	0.00
CaO	0.04	0.00	0.00	**CaO**	0.17	0.00	0.05	**SO3**	0	**CaO**	0.00	0.01	0.02	0.07	**CaO**	0.00	0.06
Na2O	0.00	0.02	0.38	**Na2O**	2.18	0.36	11.07	**Na2O**	0.09	**Na2O**	0.04	0.01	0.08	0.08	**BaO**	11.75	13.22
K2O	0.04	0.07	9.00	**K2O**	13.03	15.87	0.46	**SiO2**	0.06	**K2O**	10.78	10.58	9.61	10.33	**Na2O**	0.43	0.46
Total	86.08	85.26	93.92		99.60	98.68	99.51		99.67		94.99	92.62	93.98	94.91	**K2O**	10.94	10.43
															Total	97.86	97.89
Oxygens:	14.00	14.00	11.00		8.00	8.00	8.00				11.00	11.00	11.00	11.00		8.00	8.00
Si	2.72	2.74	2.71	**Si**	2.98	2.99	3.012			**Si**	3.47	3.38	3.24	3.40	**Si**	2.79	2.76
Ti	0.00	0.00	0.19	**Ti**	0.00	0.00	0.008			**Ti**	0.01	0.02	0.15	0.01	**Ti**	0.00	0.00
Al IV	1.28	1.26	1.73	**Al**	1.03	1.02	0.977			**Al IV**	0.53	0.63	0.76	0.60	**Al**	1.22	1.23
Al VI	1.41	1.42		**Cr**	0.00	0.00	0			**Al VI**	1.52	1.53	-0.76	-0.60	**Cr**	0.00	0.00
Cr	0.00	0.00	0.00	**Fe3**	0.00	0.00	0.006			**Cr**	0.00	0.00	0.00	0.00	**Fe3**	0.00	0.00
Fe3	0.00	0.00	0.00	**Fe2**	0.00	0.00	0			**Fe3**	0.00	0.01	0.00	0.00	**Fe2**	0.00	0.00
Fe2	2.59	2.53	1.15	**Mn**	0.00	0.00	0			**Fe2**	0.14	0.10	0.08	0.11	**Mn**	0.00	0.00
Mn	0.04	0.04	0.02	**Mg**	0.00	0.00	0.001			**Mn**	0.00	0.01	0.00	0.00	**Mg**	0.00	0.00
Mg	1.89	1.91	0.97	**Ca**	0.01	0.00	0.002			**Mg**	0.37	0.37	0.20	0.31	**Ca**	0.00	0.00
Ca	0.01	0.00	0.00	**Na**	0.19	0.03	0.942			**Ca**	0.00	0.00	0.00	0.01	**Ba**	0.24	0.27
Na	0.00	0.00	0.06	**K**	0.76	0.95	0.026			**Na**	0.01	0.00	0.01	0.01	**Na**	0.04	0.05
K	0.01	0.01	0.88							**K**	0.92	0.93	0.82	0.88	**K**	0.71	0.69
Sum	9.94	9.93	7.71	**Sum**	4.98	4.99	4.97			**Sum**	6.97	6.98	6.85	6.93	**Sum**	5.00	5.00
XMg	0.42	0.43	0.46	**XAn**	0.83	0.00	0.21			**XPg**	0.48	0.09	0.96	0.98	**XCls**	23.74	26.73
				XAb	20.12	3.37	97.11			**XMs**	50.34	56.12	72.23	57.39	**XAb**	4.30	4.60
				XOr	79.05	96.63	2.68			**XCel**	49.19	43.79	26.81	41.63	**XOr**	71.96	68.66
										Charge deficit	0.93	0.93	0.84	0.90			

Table 2: Microprobe analysis of minerals from the protolith, the cataclasite and the gouges. The structural formula were calculated with the software AX from (Holland and Powell, 2006). Ferric iron was recalculated according to the method of (Holland and Powell, 1998). Wm = White micas, Chl = Chlorite, Bi = Biotite, Fsp = Feldspars, Fap = Fluorapatite, Pg = Paragonite, Ms = Muscovite, Cel = Celadonite, An = Anorthite, Ab = Albite, Or = Orthoclase, Hy = Hyalophane, Cls = Celsian, XMg=Mg/(Mg+Fe).